

Relativistic hydrodynamics in the presence of puncture black holes

Joshua A. Faber,^{1,*} Thomas W. Baumgarte,^{2,†} Zachariah B. Etienne,¹ Stuart L. Shapiro,^{1,‡} and Keisuke Taniguchi¹

¹*Department of Physics, University of Illinois at Urbana-Champaign, Urbana, IL 61801*

²*Department of Physics and Astronomy, Bowdoin College, Brunswick, ME 04011*

(Dated: October 22, 2018)

Many of the recent numerical simulations of binary black holes in vacuum adopt the moving puncture approach. This successful approach avoids the need to impose numerical excision of the black hole interior and is easy to implement. Here we wish to explore how well the same approach can be applied to moving black hole punctures in the presence of relativistic hydrodynamic matter. First, we evolve single black hole punctures in vacuum to calibrate our BSSN (Baumgarte-Shapiro-Shibata-Nakamura) implementation and to confirm that the numerical solution for the exterior spacetime is invariant to any “junk” (i.e., constraint-violating) initial data employed in the black hole interior. Then we focus on relativistic Bondi accretion onto a moving puncture Schwarzschild black hole as a numerical testbed for our high-resolution shock-capturing relativistic hydrodynamics scheme. We find that the hydrodynamical equations can be evolved successfully in the interior without imposing numerical excision. These results help motivate the adoption of the moving puncture approach to treat the binary black hole-neutron star problem using conformal thin-sandwich initial data.

I. INTRODUCTION

The evolution of spacetimes containing black holes (BHs) has been a long-standing focus of numerical relativity. Among other astrophysical systems containing compact objects, BHs in binaries with compact object companions have long been considered promising sources of gravitational waves that can be detected by the new generation of ground-based gravitational wave interferometers LIGO [1], TAMA [2], GEO [3] and VIRGO [4], and by the proposed space-based detector LISA [5].

The recent association of short gamma-ray bursts with galaxies with extremely low star-formation rates has virtually ruled out supernovae as the progenitors of short gamma-ray bursts, and instead favors either stellar-mass black hole-neutron star (BHNS) or neutron star-neutron star (NSNS) mergers (see [6] for a review). While multiple aspects of the NSNS scenario have been studied in detail (see, e.g., [7, 8, 9, 10, 11, 12, 13] for simulations performed in general relativity), progress on BHNS mergers has been significantly slower. This is not surprising, since simulations of BHNS binaries combine the computational difficulties associated with the BH singularity with those arising from shocks and other hydrodynamic phenomena associated with the neutron star matter.

Recent advances in the numerical simulation of BHBH binaries (see [14, 15, 16] as well as numerous follow-up papers) have overcome many of the difficulties associated with the BH singularity. In particular, the “moving puncture” approach adopted by [15, 16] does not require any

excision of the BH interior, is quite easy to implement into BSSN numerical relativity schemes [17, 18], and has been used successfully in a large number of simulations. These simulations have treated the case of equal-mass, non-spinning binaries [19, 20, 21, 22, 23], and in some cases have also dealt with binaries with unequal mass [24, 25, 26], non-zero spins either aligned with the orbital angular momentum [27, 28, 29, 30] or at arbitrary orientations [31, 32, 33], or combinations of both [34, 35] (see also [36, 37, 38, 39] for alternative approaches to the BHBH problem). These puncture simulations have furnished results of great astrophysical interest, including the gravitational wave signals expected from such mergers and the kick velocities imposed on the merger remnant.

In the moving puncture approach the presence of the singularity is largely ignored, which raises the question as to why it does not spoil the numerical evolution. This issue has been clarified by [40, 41], who analyzed the geometric structure of puncture solutions. Under the gauge conditions that are used in moving puncture simulations, the dynamical evolution of a single isolated Schwarzschild BH settles down to a time slicing that terminates at a limiting surface of finite areal radius. This slicing therefore avoids the central curvature singularity, and covers only regular regions of the Schwarzschild geometry. In effect, the moving puncture approach provides a means of “excision-without-excision” (see also [42, 43] and Section II C below). An analytic expression describing the asymptotic, late-time solution has been found in [44], and we use this solution to test the convergence behavior of our code in the presence of a puncture BH.

The fact that time slices in the moving puncture approach cover only regular regions of spacetime makes it an attractive approach for modeling BHNS binaries, since then the equations of relativistic hydrodynamics – or any other matter model – can be integrated together with the gravitational field equations without any need for excision. In fact, this is the approach adopted in the

*National Science Foundation (NSF) Astronomy and Astrophysics Postdoctoral Fellow.; Electronic address: jfaber@uiuc.edu

†Also at Department of Physics, University of Illinois at Urbana-Champaign, Urbana, IL 61801

‡Also at Department of Astronomy and NCSA, University of Illinois at Urbana-Champaign, Urbana, IL 61801

only fully self-consistent dynamical simulations of orbiting BHNS binaries to date [45, 46] (see [47, 48, 49, 50] for other preliminary relativistic simulations of BHNS binaries, and [51, 52] for discussion about and simulations of alternate configurations without the use of excision).

In this paper we analyze in detail the hypothesis that relativistic hydrodynamics in the presence of puncture BHs does not require excision. As a test problem we study relativistic Bondi accretion onto a BH and compare with the analytic solution for stationary, spherical flow. We perform this test both for static and moving black holes (the latter at rest with respect to the asymptotic gas flow), and verify that the fluid behaves as expected.

This paper forms a natural stepping-stone in our group’s systematic effort to model BHNS binaries. After solving the initial value problem in general relativity [53, 54, 55, 56] and performing preliminary dynamical simulations in conformal gravitation [47, 48], we have now assembled and tested the tools to model BHNS binaries self-consistently. In contrast to [45, 46], who constructed BHNS initial data with a puncture method (see Section II B below), we plan to evolve our quasiequilibrium initial data, which we have constructed via the conformal thin-sandwich method.

Our forthcoming evolution of conformal thin-sandwich initial data raises another conceptual issue that we address in this paper. To construct quasiequilibrium BH initial data requires excising the interior and imposing suitable boundary conditions on the BH horizon [57, 58]. This approach provides data only in the black hole exterior, but the moving puncture approach for the dynamical evolution requires data in the BH interior as well. However, by definition of the BH horizon, data in the BH interior cannot affect the exterior spacetime. We demonstrate in Section III A that we can indeed replace data in the BH interior with constraint-violating “junk” data, and still find an identical evolution in the exterior. In fact, the evolution settles down to the same asymptotic late-time solution in the BH interior as well, independently of the initial data. These findings thus suggest that moving puncture simulations of BHBH binaries can adopt conformal thin-sandwich initial data, which may be less inherently eccentric and thus be more accurate approximations to true quasi-equilibrium than the puncture initial data typically used in moving puncture binary simulations [59]. This hypothesis is tested in detail in a forthcoming work [60].

This paper is organized as follows. In Sec. II, we summarize the puncture BH formalism, as well as our specific implementation of initial data, gauge conditions, matter evolution, and code diagnostics. In Sec. III, we discuss results for a number of vacuum spacetime evolutions performed for both stationary and moving puncture BHs, including calculations for which we alter the initial data in the BH interior. In Sec. IV, we present simulations of puncture BH spacetimes that contain hydrodynamic matter, and discuss how we implement a scheme that allows for stable and accurate hydrodynamical evolutions.

We conclude in Sec. V with a brief discussion of our findings.

II. NUMERICAL IMPLEMENTATION

A. The 3+1 decomposition

Throughout this paper we will cast the spacetime metric g_{ab} into the 3+1 ADM (Arnowitt-Deser-Misner) form

$$ds^2 = -(\alpha^2 - \beta_i \beta^i) dt^2 + 2\beta_i dt dx^i + \psi^4 \tilde{\gamma}_{ij} dx^i dx^j, \quad (1)$$

where α is the lapse function, β^i the shift vector, ψ the conformal factor, and $\tilde{\gamma}_{ij} \equiv \psi^{-4} \gamma_{ij}$ the conformally related spatial metric, defined so that its determinant $\tilde{\gamma} = 1$ in Cartesian coordinates. The extrinsic curvature K_{ij} is defined by

$$(\partial_t - \mathcal{L}_\beta)\gamma_{ij} = -2\alpha K_{ij}, \quad (2)$$

where \mathcal{L} denotes the Lie derivative. We note that two independent conformal rescalings of the tracefree part of the extrinsic curvature A_{ij} are widely used in the literature. In the context of initial data decompositions, this quantity is usually rescaled as

$$\bar{A}_{ij} \equiv \psi^2 \left(K_{ij} - \frac{1}{3} g_{ij} K \right), \quad (3)$$

whereas BSSN-style evolution schemes typically rescale A_{ij} as

$$\tilde{A}_{ij} \equiv \psi^{-4} \left(K_{ij} - \frac{1}{3} g_{ij} K \right), \quad (4)$$

so that its indices may be raised and lowered with the conformally related spatial metric. Our code evolves the latter expression.

We adopt the BSSN formulation [17, 18] for the dynamical evolution of the gravitational fields (see also Eqs. (11) – (15) of [61]). In addition to the quantities $\tilde{\gamma}_{ij}$, $\phi \equiv \ln \psi$, \tilde{A}_{ij} and K , this formulation utilizes the “conformal connection functions” $\tilde{\Gamma}^i \equiv -\tilde{\gamma}^{ij}_{,j}$ as auxiliary quantities. Like many BSSN implementations, we enforce the vanishing trace of \tilde{A}_{ij} and unit determinant of $\tilde{\gamma}_{ij}$ at every timestep.

B. Puncture initial data

The basic idea of puncture initial data is to factor out from the spatial metric analytic terms that represent the singular terms at a BH singularity, and treat only the remaining regular terms numerically [62, 63, 64]. Specifically, under the assumption of conformal flatness and maximal slicing, the momentum constraint decouples from the Hamiltonian constraint in the conformal transverse-traceless decomposition of Einstein’s con-

straint equations (see, e.g., [65, 66] for reviews). Moreover, the momentum constraint becomes linear and a solution representing a BH with momentum P^i is given by

$$\bar{A}^{ij} = \frac{3}{2r^2} [P^i n^j + P^j n^i - (\gamma^{ij} - n^i n^j) P^k n_k], \quad (5)$$

where r and n^i are the distance to and radial unit normal vector from the BH, and the expression is scaled as in Eq. (3). This expression can then be inserted into the Hamiltonian constraint. Decomposing the conformal factor as a sum of an analytic, singular part $\psi_s \equiv 1 + \mathcal{M}/2r$ and a term u that is regular everywhere,

$$\psi = u + \psi_s \equiv 1 + u + \frac{\mathcal{M}}{2r}, \quad (6)$$

where \mathcal{M} is a constant, the Hamiltonian constraint becomes a regular equation for u ,

$$\nabla^2 u + \frac{1}{8} \psi_s^{-7} \bar{A}^{ij} \bar{A}_{ij} (1 + u/\psi_s)^{-7} = 0. \quad (7)$$

For moving BHs, the solution for ψ can be found analytically up to second order in P^i (see, e.g., [67])

$$u = \frac{P^2}{8\mathcal{M}(\mathcal{M} + 2r)^5} [u_0(r)P_0(\mu) + u_2(r)P_2(\mu)] \quad (8a)$$

$$u_0 = \mathcal{M}^4 + 10\mathcal{M}^3 r + 40\mathcal{M}^2 r^2 + 80\mathcal{M} r^3 + 80r^4 \quad (8b)$$

$$u_2 = \frac{\mathcal{M}}{5r^3} \left(42\mathcal{M}^5 r + 378\mathcal{M}^4 r^2 + 1316\mathcal{M}^3 r^3 + 2156\mathcal{M}^2 r^4 + 1536\mathcal{M} r^5 + 240r^6 + 21\mathcal{M}(\mathcal{M} + 2r)^5 \ln\left(\frac{\mathcal{M}}{\mathcal{M} + 2r}\right) \right), \quad (8c)$$

where $P_0(\mu) = 1$ and $P_2(\mu) = 3\mu^2/2 - 1/2$ are Legendre polynomials and $\mu \equiv \cos\theta$. Clearly, for static BHs with $P^i = 0$ we find $u = 0$ as expected, and recover a Schwarzschild $t = \text{const.}$ slice in isotropic coordinates. We also note that the parameter \mathcal{M} in the above equations reduces to the BH ADM mass only for static BHs (see also Section II G below).

C. Moving puncture evolutions

The success of the puncture method for initial data suggests that a similar approach might be equally successful for dynamical evolutions. However, the original puncture method – namely, factoring out analytical singular terms and evolving the remaining regular terms alone – did not achieve long-term stable evolutions in dynamical simulations (see, e.g., [68, 69]). The problem may be associated with the need for a coordinate system that leaves the puncture at a prescribed location in the numerical grid, given by the singularity in the analytical function. The breakthrough in the recent dynamical puncture simulations is based on using a “moving” puncture in which no singular term is factored out [15, 16].

With suitable coordinate conditions (see Section II D below), this prescription leads to remarkably stable evolutions. This is somewhat surprising, since one might have expected the presence of singularities to spoil the numerical evolution. This issue has been clarified recently by [40, 41], who analyzed the geometric structure of puncture solutions.

For a single isolated BH at rest in the coordinate system, initial data representing a slice of constant Schwarzschild time in isotropic coordinates are given by Eq. (6) with $u = 0$. Isotropic coordinates do not penetrate the BH horizon, and instead cover two copies of the BH exterior that can be thought of as two different asymptotically flat universes connected by an Einstein-Rosen bridge. The conformal factor Eq. (6) diverges at $r = 0$; this point corresponds to the asymptotically flat end of the “other” universe, and hence is a relatively harmless coordinate singularity only. This initial slice does not encounter the BH spacetime singularity.

With the gauge conditions typically used in moving puncture simulations, such initial data lead to an episode of “dynamical” evolution until the solutions settle down to a new equilibrium state. Specifically, in the adopted gauge the metric coefficients depend on time, and hence appear dynamical until they settle down. In the new equilibrium state the conformal factor is still singular at $r = 0$, but it now features a $1/\sqrt{r}$ singularity instead of the previous $1/r$ coordinate singularity. Such behavior indicates that the point $r = 0$ now represents a limiting surface of finite areal radius R_{areal} . The slice has thus disconnected from the other asymptotically flat end, and instead terminates on a surface of finite R_{areal} inside the BH’s horizon. The numerical grid does not include the spacetime singularity at $R_{\text{areal}} = 0$, so that the point $r = 0$ is again a coordinate singularity only. This helps explain the success of this numerical method, which, in short, may be thought of as “excision-without-excision” (see also [42] for an explanation of this numerical behavior).

This realization about puncture geometry suggests that it should be straightforward to extend the puncture approach to describe relativistic hydrodynamics in the presence of BHs. The numerical grid covers only regular regions of the spacetime, so the fluid cannot encounter any spacetime singularities. At $r = 0$, which corresponds to a sphere of finite areal radius R_{areal} inside the horizon, all field and fluid characteristics point inward to smaller areal radii. The interior of the sphere may therefore be disregarded – it cannot affect the exterior. As we will discuss in Section II E below, finite differencing around the point $r = 0$ can lead to numerical error that complicates some of our expectations; however, this is a purely numerical issue that can be dealt with quite straightforwardly.

D. Gauge and boundary conditions

The key to the success of a moving puncture evolution is the identification of suitable gauge conditions. Both [15] and [16] use an advective “1+log” slicing condition for the lapse

$$\partial_t \alpha - \beta^i \partial_i \alpha = 2\alpha K. \quad (9)$$

The advection term forces the singularity, located at the point where $\psi \rightarrow \infty$ and $\alpha \rightarrow 0$, to move with coordinate velocity $v^i \equiv dx^i/dt = -\beta^i$. We note that we evaluate all advective terms $\beta^i \partial_i$ using “upwind” differencing, as described in [70].

The gauge condition used in moving puncture evolutions is a hyperbolic “gamma-driver” condition for the shift, either

$$\partial_t \beta^i - \beta^j \partial_j \beta^i = \frac{3}{4} B^i, \quad (10a)$$

$$\partial_t B^i - \beta^j \partial_j B^i = \partial_t \tilde{\Gamma}^i - \beta^j \partial_j \tilde{\Gamma}^i - \eta B^i, \quad (10b)$$

or

$$\partial_t \beta^i = \frac{3}{4} B^i, \quad (11a)$$

$$\partial_t B^i = \partial_t \tilde{\Gamma}^i - \eta B^i. \quad (11b)$$

The former choice is referred to in [71] as the “shifting-shift” condition, and represents the choice $\zeta_S = \zeta_b = \zeta_f = 0$ in the notation of [72], who studied the hyperbolicity of the resulting evolution scheme. The latter is referred to as the “non-shifting-shift”, and has $\zeta_S = \zeta_b = \zeta_f = 1$. We note that [45] use a modified, first-order version of the non-shifting-shift with a differential stabilization term. Throughout this work, we will use only the “non-shifting-shift”, Eqs. (11a) and (11b).

The term η in Eqs. (10b) and (11b), which has units of \mathcal{M}^{-1} , is a damping term that has a non-trivial effect on the evolution of the puncture as it moves across the grid. In general, for larger values of η , the BH has a smaller coordinate velocity but a larger coordinate radius, which allows for better numerical resolution of the BH horizon. However, larger values of η were shown in [71] to produce significantly larger values of $\tilde{\Gamma}^i$, indicating a stronger deformation of the metric during the evolution. This is often disadvantageous, especially with regard to specifying boundary conditions. We use $\eta = 0.25/\mathcal{M}$ for the static BHs in Sec. III A, $\eta = 0.2/\mathcal{M}$ for matter evolutions in Sec. IV, but $\eta = 2.0/\mathcal{M}$ for moving black holes in Secs. III B 1 and III B 2 so that we can directly compare with the results of [71].

For our runs with relatively close outer boundaries described in Sec. III A we use Robin-type boundary conditions for our metric and field variables, assuming a $1/r$ falloff behavior away from their asymptotic values. For larger runs we employ outgoing wavelike boundary conditions, based on the local speed of light and again assuming a $1/r$ falloff. The conditions are slightly modified when we use a “fisheye” coordinate scheme, as we discuss in Appendix A.

E. Hydrodynamics

Our hydrodynamics scheme is essentially identical to the grid-based, fully general relativistic, high resolution shock capturing scheme described in [73], although here we do not include any electromagnetic terms in our evolution calculations. This scheme for both matter and field evolution is based on second-order finite differencing, which we have now embedded within the *Cactus* grid hierarchy [74].

We assume a stress energy tensor in the form $T^{\mu\nu} = \rho_0 h u^\mu u^\nu + P g^{\mu\nu}$ where ρ_0 is the rest density, h the specific enthalpy, and u^μ the 4-velocity of the fluid. We will also assume a gamma-law equation of state

$$P = (\Gamma - 1)\rho_0 \epsilon, \quad (12)$$

where ϵ is the specific internal energy.

In our numerical code, we evolve the “conserved” quantities ρ_* , \tilde{S}_i , and $\tilde{\tau}$, defined by Eqs. (36) and (37) of [73]. These conserved quantities are defined in terms of the “primitive” variables ρ , v^i , and P , according to their Eqs. (41) – (43). The transformation from the conserved quantities back to the primitive set requires an iteration (see Eqs. (59) – (62) of [73]).

We find that this iteration is very accurate everywhere except in the region immediately surrounding the puncture, where accumulated errors in the finite differencing can lead to unphysical values of the primitive variables. To overcome this difficulty, we note that the quantity $\tilde{\tau}$, which serves as the energy variable in the conserved set of variables, should always remain positive. In fact, it has to remain greater than $w - \rho_*$, where $w \equiv \alpha u^0 \rho_*$, in order to satisfy $h \geq 1$ (see Eq. (58) in [73]), but positivity is sufficient for our purposes. To enforce this, we set $\tilde{\tau}$ to a minimum value, typically $\tilde{\tau} = 10^{-3}$ whenever it would otherwise be negative. Furthermore, from (58) in [73] we see that in the limit $h \rightarrow 1$ we have $w \rightarrow \tilde{\tau} + \rho_*$, or equivalently

$$|\tilde{S}|^2 \equiv \gamma^{ij} \tilde{S}_i \tilde{S}_j \rightarrow \tilde{\tau}(\tilde{\tau} + 2\rho_*). \quad (13)$$

It can be shown that this limit on $|\tilde{S}|^2$ is an upper limit. When numerical error leads to a value of $|\tilde{S}|^2$ that is larger than the allowed value, we enforce this condition by reducing the magnitude of \tilde{S}_i so that $|\tilde{S}|^2$ is reduced to $0.98 \times \tilde{\tau}(\tilde{\tau} + 2\rho_*)$, leaving the ratios of the individual vector components unchanged.

We again point out that the above “fixes” are employed only in the immediate vicinity of the puncture, inside the BH horizon. The need for these fixes arises from poor resolution around the puncture and the resulting large finite differencing error. We find that increasing the grid resolution decreases the size of the region in which the fixes are needed. Other than dealing with this break-down in the iteration between conserved and primitive fluid variables, the equations of relativistic hydrodynamics can be integrated without need for excision in the presence of puncture black holes.

F. Coordinates

We perform simulations both in 2+1 (i.e., axisymmetry) and in 3+1, using the HRSC, BSSN code of [73], which accommodates both cases. Our 2+1 simulations adopt the "cartoon" method for the fields, as described in [75].

Finite difference simulations with fixed spatial resolution in three spatial dimensions are very intensive computationally, since they simultaneously require a fine grid resolution close to the BH, and boundary conditions imposed at a sufficiently large separation. We have implemented so-called "fisheye" coordinates to solve the problem of dynamic range (see [15]). In Appendix A we review the coordinate transformation and its effect on the various terms that appear in our numerical scheme, especially our shift evolution equation.

G. Diagnostics

We monitor several global quantities computed from surface integrals at large separations. These include the ADM mass

$$M_{\text{ADM}} = \frac{1}{2\pi} \int (\tilde{\Gamma}^i/8 - \gamma^{ij} \partial_j \psi) d\Sigma_i, \quad (14)$$

and the linear momentum

$$P_j = \frac{1}{8\pi} \oint (K_j^i - \delta_j^i K) d\Sigma_i, \quad (15)$$

where $d\Sigma_i = (x^i/r)\psi^6 r^2 \sin\theta d\theta d\phi$ for a spherical surface at fixed radius.

We also compute the irreducible mass of the BH from

$$M_{\text{irr}} = \sqrt{\mathcal{A}/16\pi}. \quad (16)$$

Instead of computing the proper area \mathcal{A} of the BH's event horizon, we approximate this area as that of the apparent horizon.

For the approximate boosted BH solutions of Section II B the ADM mass and irreducible mass are related to the parameter \mathcal{M} , to leading order in P^i , by

$$M_{\text{ADM}} = \mathcal{M} + \frac{5}{8} \frac{P^2}{\mathcal{M}}, \quad M_{\text{irr}} = \mathcal{M} + \frac{1}{8} \frac{P^2}{\mathcal{M}}, \quad (17)$$

(see [76]). Throughout this paper we express dimensional quantities in units of \mathcal{M} .

III. VACUUM TESTS

To test the vacuum sector of our puncture code, we have performed a suite of tests for stationary and moving puncture BHs, both in 2+1 and 3+1. In these tests we adopt two slightly different slicing conditions, namely the 1+log condition Eq. (9), both with and without the

advective term $\beta^i \partial_i \alpha$. Most commonly, moving puncture solutions employ condition Eq. (9) with the advective term; we will refer to this condition as "advective 1+log" slicing. The geometry of the resulting spacetime has been analyzed in [40]. In [41], the authors considered dropping the advective term, which results in the "non-advective 1+log" slicing

$$\partial_t \alpha = -2\alpha K. \quad (18)$$

As it does for the advective 1+log slicing, the dynamical evolution using the modified slicing condition quickly settles down to a new equilibrium, but in this case this time-independent solution must evidently be maximally sliced with $K = 0$. As it turns out, this maximally sliced asymptotic solution can be found analytically (see [44]). In Section III A we therefore perform tests comparing with the analytic solution, before considering the more common advective 1+log slicing in Section III B.

A. Non-advective 1+log slicing

As demonstrated in [41], dynamical puncture evolutions with the non-advective 1+log slicing condition Eq. (18) settle down to a maximally sliced, time-independent solution, given analytically by Eqs. (11)-(15) of [44]. We test our code by comparing the late-time solution of dynamical puncture evolutions with the analytical solution. In these tests we consider three different types of initial data, which we summarize in Table I. In the first set of runs, labeled by "BN" in Table I, we adopt the analytical solution of [44] itself as initial data. The second set of runs, labeled by "ISO", adopts as initial data a $t = \text{const.}$ time slice of the Schwarzschild solution in isotropic coordinates, given by Eq. (6) for $u = 0$, together with $\alpha = \psi^{-2}$. The third set of initial data is identical to the second set in the BH exterior, but now we replace the interior data with some constraint-violating "junk". We adopt these data to test whether we can use initial data that only provide valid exterior data in puncture evolutions, which also require initial data to fill the arrays in the interior. We consider three different choices for the interior solution. In the first choice, labeled "Horizon Junk" or "HJ", we set the values of the conformal factor and lapse function throughout the interior of the BH to their values on the horizon, i.e. $\psi = 2$ and $\alpha = 1/4$ for $r < r_h \equiv \mathcal{M}/2$. For the second choice, labeled "Interior Junk" or "IJ", we again set ψ and α to constant values, but this time only inside $r_h/2$, so $\psi = 3$ and $\alpha = 1/9$ for $r < r_h/2$, using the isotropic solution everywhere outside this. Finally, in our third choice, labeled "Smooth Junk" or "SJ", we construct an even, fourth-order polynomial in the BH interior that joins on to the exterior conformal factor in such a way that the function and its first two derivatives are continuous on the horizon. Specifically, we choose $\psi = 2.875 - 5(r/\mathcal{M})^2 + 6(r/\mathcal{M})^4$ in the BH interior, and $\alpha = \psi^{-2}$.

TABLE I: Summary of our stationary vacuum puncture simulations discussed in Sec. III A. “Baumgarte & Naculich” refers to the analytical solution of [44]; our different “junk” initial data are described in the text.

Name	Initial Data	Resolution	Grid
2+1; no fisheye; $ x^i \leq 15M$			
BN2a	Baumgarte & Naculich	$\mathcal{M}/32$	480×480
BN2b	Baumgarte & Naculich	$\mathcal{M}/24$	360×360
BN2c	Baumgarte & Naculich	$\mathcal{M}/16$	240×240
BN2d	Baumgarte & Naculich	$\mathcal{M}/8$	120×120
HJ2a	Isotropic “Horizon Junk”	$\mathcal{M}/32$	480×480
ISO2a	Isotropic Schwarzschild	$\mathcal{M}/32$	480×480
3+1; fisheye, $ \bar{x}^i \leq 6M \rightarrow x^i < 15M$			
ISO3	Isotropic Schwarzschild	$\mathcal{M}/16$	$192^2 \times 96$
IJ3	Isotropic “Interior Junk”	$\mathcal{M}/16$	$192^2 \times 96$
HJ3	Isotropic “Horizon Junk”	$\mathcal{M}/16$	$192^2 \times 96$
SJ3	Isotropic “Smooth Junk”	$\mathcal{M}/16$	$192^2 \times 96$

All simulations described in this Section were performed using equatorial symmetry. For 3+1 runs we used fisheye coordinates with parameters $a_0 = 1$, $a_1 = 4$, $R_1 = 3$, $s_1 = 1.0$. While we always employ a cubic coordinate grid, a cubic grid in fisheye coordinates does not correspond to a cubic grid in physical coordinates. Thus, the boundaries we quote in physical coordinates only apply at the coordinate axes, and lie further out at other angles. When we quote a numerical resolution for a given run, it refers to the central region of the fisheye transition, for which the physical and fisheye coordinates essentially overlap. The numerical resolution with respect to physical coordinates will be more coarse at larger radii, by construction. In all calculations described in this section, we set $\eta = 0.25/M$ in the shift evolution equation. All evolutions described in this Section were terminated at $t_F = 300M$.

We first compare the “BN2” simulations at four different grid resolutions to establish second-order convergence of our code. In the top panel of Fig. 1, we show the absolute deviations between our numerical runs at $t = 10M$ and the exact solution for run BN2a at resolution $\mathcal{M}/32$ (solid), BN2b at $\mathcal{M}/24$ (dotted), BN2c at $\mathcal{M}/16$ (dashed), and BN2d at $\mathcal{M}/8$ (dot-dashed), focusing on the inner region of the grid, where deviations are most apparent, and which, at $t = 10M$, is causally disconnected from the outer boundary at $15M$. To confirm the expected second-order convergence we show the same quantities in the bottom panel rescaled by factors of 16, 9, 4, and 1, respectively.

We now compare the late-time solution as it emerges from our three different types of initial data. In Fig. 2 we show results for runs BN2a, ISO2a and HJ2a, which all have the same grid resolution. Evidently, all late-time solutions agree very well with the analytical solutions. The deviation from the analytical solution is at most about 1% for all three runs, and is caused by finite difference

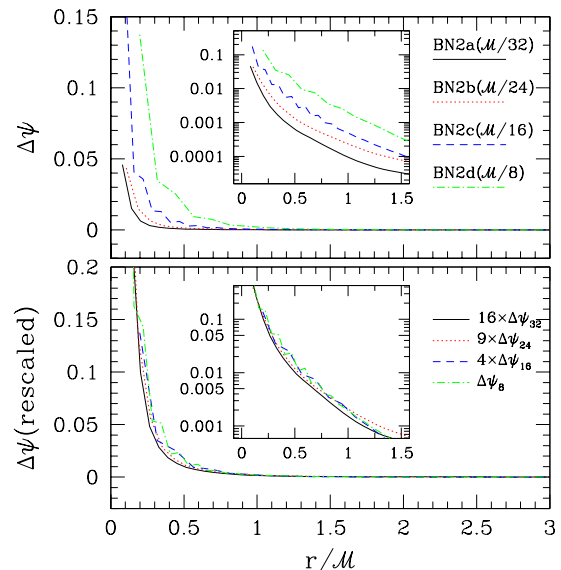


FIG. 1: Deviations from the exact solution for the conformal factor $\Delta\psi$ for the runs BN2 (see Table I). The top panel shows the deviations themselves, while in the lower panel the deviations are appropriately rescaled to demonstrate second-order convergence.

error as well as the outer boundary. To within these numerical errors, all three late-time solutions agree with each other, even if we replace the interior initial data with junk that does not even satisfy the constraints. It is particularly noticeable that even in the BH interior no “memory” of this junk remains at this late time, and that the solution approaches the analytically known late-time solution throughout.

While it is not surprising that data in the BH interior does not affect the exterior solution, it is reassuring to see that this holds true even in a numerical simulation. To further illustrate this point we performed the 3+1 simulations ISO3, HJ3, IJ3, and SJ3, and plot the ADM mass as a function of time in the top panel Fig. 3. We find excellent agreement with the stationary solution at late times for these runs, indicating that information contained in the BH interior does not affect the exterior solution as we evolve. In quantitative terms, applying junk either within the horizon or smoothly at the horizon results in a change in the ADM mass of 0.05%, as we show in the bottom panel of the Figure. We note that reflections off the outer boundary are at least partially responsible for the discrepancy, given the time at which they appear. To confirm the proper behavior of our code when we have constraint-violating junk in the BH interior, we show in Fig. 4 the convergence of the ADM mass for stationary puncture runs using smooth junk, performed at numerical resolutions of $\mathcal{M}/20$, $\mathcal{M}/16$, and $\mathcal{M}/12$. The lower panel suggests self-consistent second-order convergence at all times. At both early and late times, we have also verified that the code converges at second-order to the analytic solution ($M_{\text{ADM}} = 1$); at intermediate times we

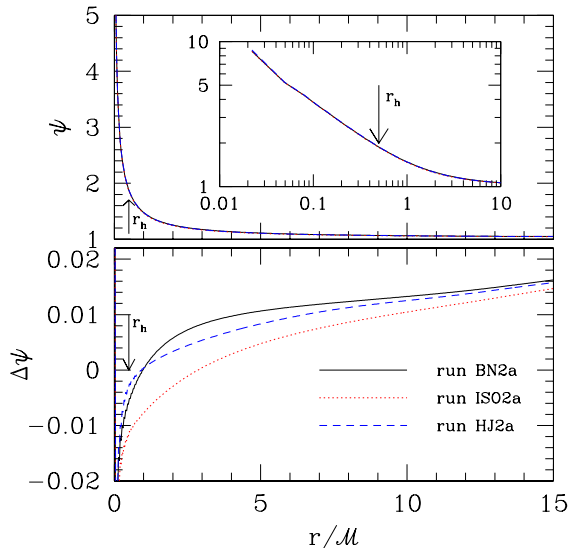


FIG. 2: The top panel shows profiles of the conformal factor ψ at $t = 300M$ for runs BN2a, ISO2a and HJ2a (see Table I). All simulations are performed with a grid spacing of $M/32$, using the gauge condition Eq. (18), for which the late-time solution is known exactly. In the bottom panel we show the absolute deviations between our numerical results and the exact solution, finding that they are small throughout. The arrows mark the location of the apparent horizon.

find a brief departure from this behavior that is likely caused by reflections off the outer boundary. Even for the simulation HJ3, where the “junk” joins the exterior with discontinuous derivatives on the horizon, the ADM mass deviates from the ISO3 simulations by only 1% over the course of the evolution. These simulations indicate that the evolution is relatively insensitive to the details of the initial data in the BH interior, even when the differencing stencil in the exterior of the BH overlaps non-differentiable regions. Still, our results clearly suggest that only smoothly extrapolated data should be used in dynamical evolution calculations.

Our “junk” tests suggest a very simple solution to the following conceptual issue. Many sets of initial data describing compact binaries are constructed with the conformal thin-sandwich decomposition. For the construction of BHs, these equations are supplemented with equilibrium boundary conditions that are imposed on the BHs’ horizons. As a consequence, these data describe only the exterior geometry, and do not provide any initial data for the BH interior. Evolution calculations that employ the moving puncture approach do not excise the BHs, and hence require initial data that extend into the BH interior. Our tests suggest that we can nevertheless use excised initial data, e.g., conformal thin-sandwich data, and simply fill the BH interior with some arbitrary but sufficiently smooth “junk”. This is the approach that we plan to adopt for simulations of mixed BHNS binaries, enabling us to use our quasi-equilibrium models [55, 56]

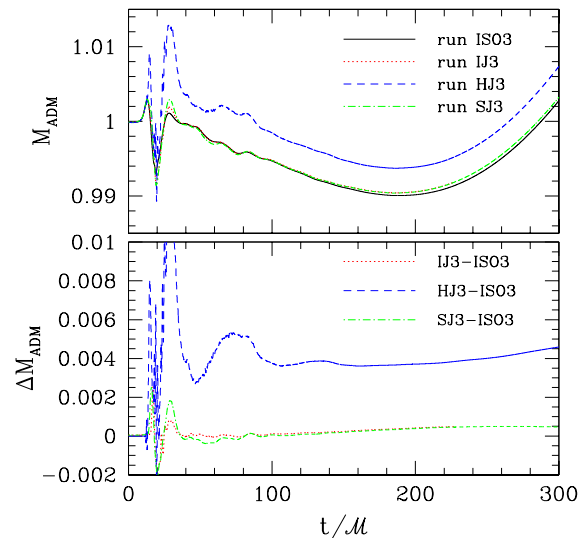


FIG. 3: The ADM mass (14) for the 3+1 runs using fish-eye and $M/16$ numerical resolution in the central region (top panel). We show results for initial data ISO3, IJ3, HJ3 and SJ3 (see Table I). In the bottom panel, we plot the differences between the ADM mass from the junk runs and that of run ISO3. We see a deviation of .05% between run ISO3 and runs IJ3 and SJ3 over the course of the run, indicating that the evolution is insensitive to the initial data in the BH interior.

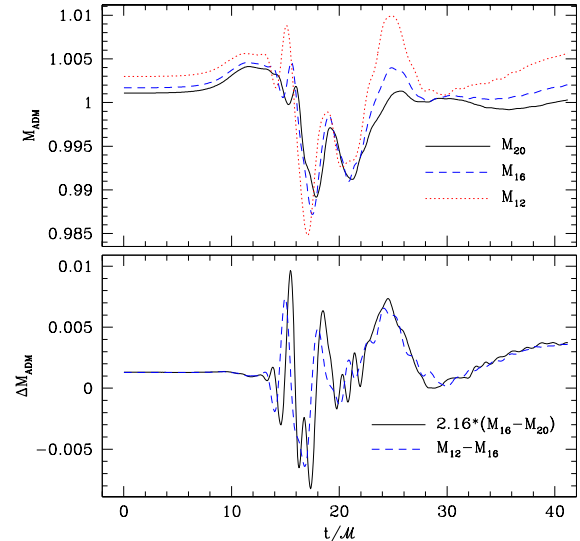


FIG. 4: The top panel shows the ADM mass measured at a radius $r = 12.1M$, for runs with smooth junk as initial data and numerical resolutions of $M/20$, $M/16$, and $M/12$. In the bottom panel, the differences between the runs are rescaled to demonstrate second-order convergence.

as initial data.

TABLE II: Vacuum evolution runs discussed in Secs. III B 1 and III B 2.

Name	Initial Data	Grid	Resolution	t_F
2+1 w/Fisheye; $ \bar{x}_{fish}^i \leq 15\mathcal{M}$, $ x^i \leq 136\mathcal{M}$				
SP2a	Stat. Punc.	360×360	$\mathcal{M}/24$	$100\mathcal{M}$
SP2b	Stat. Punc.	240×240	$\mathcal{M}/16$	$100\mathcal{M}$
SP2c	Stat. Punc.	120×120	$\mathcal{M}/8$	$100\mathcal{M}$
3+1 w/Fisheye; $ \bar{x}_{fish}^i \leq 12\mathcal{M}$, $ x^i \leq 88\mathcal{M}$				
SP3a	Stat. Punc.	$240^2 \times 120$	$\mathcal{M}/10$	$100\mathcal{M}$
SP3b	Stat. Punc.	$192^2 \times 96$	$\mathcal{M}/8$	$100\mathcal{M}$
SP3c	Stat. Punc.	$144^2 \times 72$	$\mathcal{M}/6$	$100\mathcal{M}$
2+1 w/o Fisheye; $P^i = 0.5$, $ x^i \leq 70\mathcal{M}$				
MP2a ^a	Mov. Punc.	1760×3520	$\mathcal{M}/32$	$50\mathcal{M}$
MP2b	Mov. Punc.	1680×3360	$\mathcal{M}/24$	$50\mathcal{M}$
MP2c	Mov. Punc.	1120×2240	$\mathcal{M}/16$	$50\mathcal{M}$
MP2d	Mov. Punc.	560×1120	$\mathcal{M}/8$	$50\mathcal{M}$
3+1 w/Fisheye; $P^i = 0.5$, $ \bar{x}_{fish}^i \leq 14\mathcal{M}$, $ x^i \leq 120\mathcal{M}$				
MP3a	Mov. Punc.	$336^2 \times 168$	$\mathcal{M}/12$	$50\mathcal{M}$
MP3b	Mov. Punc.	$280^2 \times 140$	$\mathcal{M}/10$	$50\mathcal{M}$
MP3c	Mov. Punc.	$224^2 \times 112$	$\mathcal{M}/8$	$50\mathcal{M}$
MP3d	Mov. Punc.	$168^2 \times 84$	$\mathcal{M}/6$	$50\mathcal{M}$

^aFor this run, $|x^i| \leq 55\mathcal{M}$

B. Advective 1+log slicing

The lapse evolution equation used in Sec. III A above is useful since it leads to an analytically known solution for a single BH. However, most moving puncture simulations of binaries employ the advective 1+log slicing Eq. (9) which allows the punctures to move through the numerical grid. We now study evolutions with this advective 1+log slicing, both for stationary and moving BHs. Our simulations are summarized in Table II, where ‘‘SP’’ refers to stationary puncture solutions, described in more detail in Section III B 1, and ‘‘MP’’ stands for moving puncture solutions, described in Sec. III B 2. For purposes of comparison with the results of [71] (see Sec. III B 2) we set $\eta = 2.0/\mathcal{M}$ in Eq. (11b) for all of the results discussed in this Section.

1. Stationary black holes

For our stationary puncture simulations we choose a double fisheye coordinate system with parameters $a_0 = 1$, $a_1 = 4$, $a_2 = 16$, $R_1 = 4.5\mathcal{M}$, $R_2 = 7.5\mathcal{M}$, and $s_1 = s_2 = 1.5\mathcal{M}$ (see Appendix A). Our initial data are $t = \text{const.}$ slices of the Schwarzschild metric expressed in isotropic coordinates, like the ‘‘ISO’’ data of Table I. We adopt the gauge conditions Eqs. (11a) and (A15) and evolve to a time $t_F = 100\mathcal{M}$. By this time the solution has settled down into the late-time equilibrium solution, and further evolution would lead to only very small changes in the fields. We use three different grid resolutions for both

our 2+1 and 3+1 simulations to study the convergence behavior of our code as indicated in Table II.

In the top panel of Fig. 5, we show the ADM mass for our highest resolution 3+1 calculation, run SP3a, measured at $\bar{r}_{\text{int}} = 5.8, 6.8, 7.9$, and 9.0 . Similarly, in the bottom panel we show the ADM mass for our highest resolution axisymmetric calculation, run SP2a. We see two phenomena: first, at a time roughly corresponding to $t = r_{\text{int}}$, we see a small, temporary glitch in the ADM mass for each value of r_{int} , followed by a slow deviation from the exact value. This indicates the passage of junk gravitational radiation, present in the initial data only because of numerical errors associated with discretization, through the surface, and is generic to calculations like these. Second, we note that our results converge as we move the integration surface outward, as we would expect. This is true both before and after the passage of the junk radiation through the surface. For the outermost surface, we see a variation in the ADM mass of no more than half a percent over an integration time of $100\mathcal{M}$. In general, we find that the late time deviations from the exact ADM mass scale like r_{int}^{-4} through most of our grid.

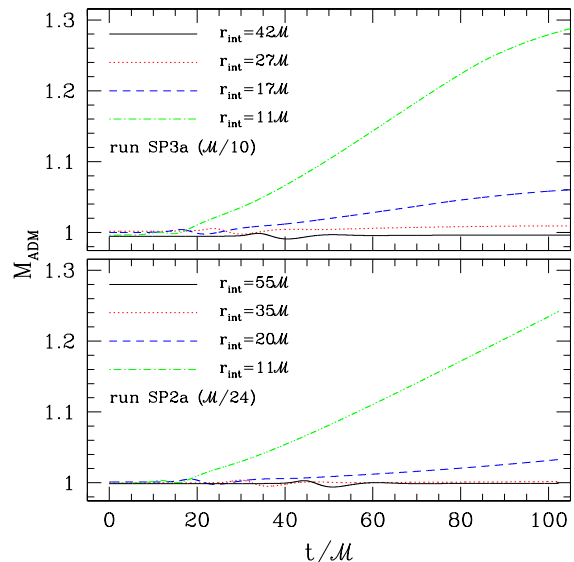


FIG. 5: ADM mass versus time for stationary puncture evolutions, measured using Eq. (14) at surfaces of different radii. In the top panel, we show results for surfaces at constant fisheye radius $\bar{r} = 5.8$ (dot-dashed), 6.8 (dashed), 7.9 (dotted), and 9.0 (solid) in 3+1 run SP3a, which correspond to physical radii $r_{\text{int}} = 11\mathcal{M}, 17\mathcal{M}, 27\mathcal{M}$, and $42\mathcal{M}$, respectively. In the bottom panel, the integration surfaces are placed at $\bar{r} = 5.8, 7.2, 8.5$, and 9.9 , corresponding to physical radii $r_{\text{int}} = 11.1\mathcal{M}, 19.9\mathcal{M}, 35.2\mathcal{M}$, and $55.2\mathcal{M}$ in 2+1 axisymmetric run SP2a. For the outermost surfaces, we see deviations of less than half a percent over the course of the entire evolution in each case.

To confirm convergence, we calculate the difference of the ADM mass from its analytical value as a function

of time for all the stationary puncture runs described in Table II. In the 3+1 case, we take data from the integration surface placed at $r_{\text{int}} = 41.6$, whereas for the 2+1 case we choose the surface with $r_{\text{int}} = 55.2$. In Fig. 6, we see the proper behavior for both the 3+1 and 2+1 runs (top and bottom panels, respectively), confirming that our field evolution is indeed convergent to second order in the grid spacing. In the upper sub-panels, we show the expected convergence against the exact solution. In both the 3+1 and 2+1 simulations, numerical errors inherent in the finite-differenced initial data reach the integration surfaces at a time $t \approx r_{\text{int}}$. During the passage of oscillation, we still see second-order convergence in the differences between runs, plotted in the bottom sub-panels of each figure. Note that in the top panel, we rescale the higher resolution pair by a factor $(6^{-2} - 8^{-2}) / (8^{-2} - 10^{-2}) = 2.16$, whereas in the bottom panel the rescaling factor is $(8^{-2} - 16^{-2}) / (16^{-2} - 24^{-2}) = 5.4$.

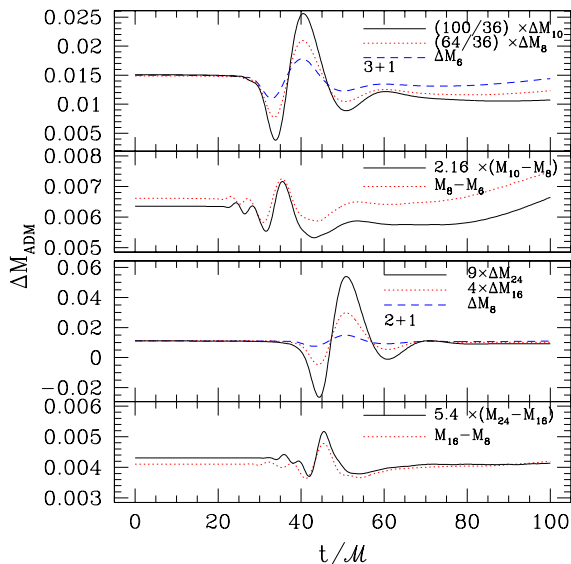


FIG. 6: Differences in exact and numerical values for the ADM mass for our SP simulations of different numerical resolution as a function of time (see Table II). In the top panel we show results for 3+1 simulations, with the ADM mass computed at $r_{\text{int}} = 41.6\mathcal{M}$. In the upper subpanel, results for different resolutions are properly rescaled to demonstrate second-order convergence against the exact solution. In the lower subpanel, we compare the differences between pairs of runs to demonstrate second-order convergence even during the passage of a spurious oscillation caused by initial errors through the data at r_{int} . The bottom panel shows similar results for 2+1 simulations, with the ADM mass computed at $r_{\text{int}} = 55.2\mathcal{M}$. Conventions are as above.

Finally, in Fig. 7, we show the irreducible mass (see Eq. (16)) of the BH as a function of time for our 3+1 (top panel) and 2+1 (bottom panel) runs, for all three numerical resolutions in both cases. To determine the location and parameters describing the apparent horizon

we use the Cactus thorn **ahfinder** [77]. We see that our results improve with increased resolution for both the 2+1 and 3+1 simulations, as shown in the upper sub-panels. For our highest resolutions in the two cases, the deviation from the exact value are smaller than 0.5% and 2%, respectively. In the lower subpanels, we show differences between results for varying numerical resolutions, demonstrating second-order convergence until the horizon finder begins to show errors at late times for our lowest-resolution runs.

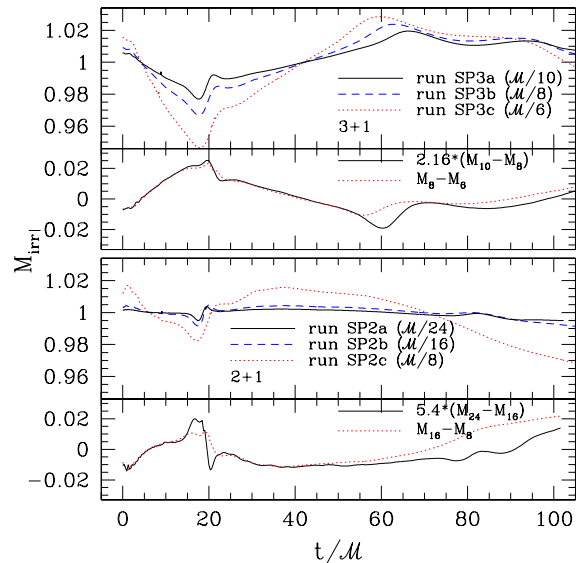


FIG. 7: Irreducible mass as a function of time for our SP runs (upper subpanels; see Table II). For our highest resolution runs in 3+1 and 2+1, we see deviations of at most 2% and 0.5%, respectively. In the lower subpanels, we show the rescaled differences between pairs of runs, demonstrating second-order convergence.

2. Moving Black Holes

We now turn to moving BH solutions. In particular, we consider the parameters discussed in detail in [71], a BH with linear momentum $P_x = 0.5\mathcal{M}$, traveling along the x-axis, starting from an initial location $x_0 = -3\mathcal{M}$. For our initial data, we calculate the extrinsic curvature and conformal factor from Eqs. (5), (6), and (8a) – (8c). We set the lapse initially to $\alpha(t=0) = \psi^{-2}(t=0)$, and the shift to zero. The spatial metric is initially conformally flat. According to (17), the ADM mass of this configuration is approximately $M_{\text{ADM}} = 1.15625\mathcal{M}$, with the leading-order error term appearing at order P^4 .

We use unigrid simulations for easier comparison with the results of [71], since the transformation to fisheye coordinates would introduce new terms into the shift equations (namely Eq. (A15) instead of Eq. (11b)). Unigrid simulations are impractical in 3+1, so we perform axisymmetric simulations instead. We choose a numerical

grid that extends twice as far along the symmetry axis as it does radially. We note that while runs MP2b, MP2c, and MP2d, with numerical spacings $\mathcal{M}/24$, $\mathcal{M}/16$ and $\mathcal{M}/8$, respectively, use a grid that extends to $r = \pm 70\mathcal{M}$ along the symmetry axis (along which the BH moves) and $r = 70\mathcal{M}$ along the radial axis, our highest resolution calculation, run MP2a with spacing $\mathcal{M}/32$, only extends to $r = 55\mathcal{M}$ in both directions. We also perform 3+1 simulations of moving punctures, which do use fish-eye coordinates. The parameters for these coordinates are the same as in Sec. III B 1, except that we choose $R_1 = 6\mathcal{M}$ and $R_2 = 9\mathcal{M}$ here to create a larger central region through which the BH travels. We evolve our moving puncture configurations until $t_F = 50\mathcal{M}$, during which time the BH remains inside the central fish-eye region.

We show the ADM mass measured at various radii for our highest resolution 3+1 and 2+1 simulations, MP3a and MP2a, in the top and bottom panels of Fig. 8. We again find better agreement between the measured ADM mass and the exact value when we evaluate Eq. (14) at larger radii.

Conservation of the ADM mass for moving punctures is comparable to that for stationary punctures, at approximately 1% over a duration $t = 50\mathcal{M}$. Some of the initial deviations for the ADM mass in the 3+1 case, visible especially for the innermost surface, are a result of small numerical errors associated with converting $\tilde{\Gamma}^i$ back into the physical value $\tilde{\Gamma}^i$ through a coordinate transformation (see Appendix A).

As before, we confirm that the ADM mass converges to second order. In the top panel of Fig. 9, we show the ADM mass measured at a surface of radius $r_{\text{int}} = 62\mathcal{M}$ as a function of time for our four 3+1 runs performed using different numerical resolutions. As can be seen in Fig. 9, the values for the ADM mass slowly drift to larger values. We speculate that this is a result of the constraints equations being solved only to order P^2 , which introduces a small but non-zero error. Instead of testing convergence to the approximate value of the ADM mass, we perform a self-consistence convergence test by computing the difference in the ADM mass between pairs of runs in the bottom panel of the figure, scaling the results appropriately in each case. In terms of the difference between lowest resolution pair, we scale the highest resolution pair by a factor $(6^{-2} - 8^{-2})/(10^{-2} - 12^{-2}) = 3.97$ and the medium resolution pair by a factor $(6^{-2} - 8^{-2})/(8^{-2} - 10^{-2}) = 2.16$. Our findings suggest second-order convergence throughout the evolution, even though at times after $t=30\mathcal{M}$ the analysis is complicated by small-amplitude numerical errors arising from discretization across fish-eye transition regions.

Combining the results from Figs. 8 and 9, we can extrapolate our results to both asymptotic radii and infinite numerical precision. With respect to the radius, we take our results at $t = 0$ measured at $r = 43\mathcal{M}$ and $62\mathcal{M}$ for run MP3a, and assume leading-order $1/r$ falloff

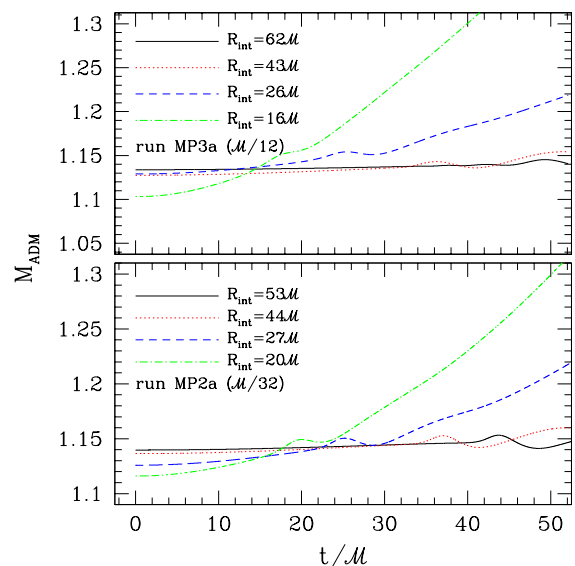


FIG. 8: ADM mass versus time for moving puncture 3+1 evolution MP3a (see Table II), measured using Eq. (14) at surfaces of different radii. In the top panel, we show results for surfaces at constant fisheye radius $\bar{r} = 8.0$ (dot-dashed), 9.2 (dashed), 10.5 (dotted), and 11.8 (solid), which correspond to physical radii $r_{\text{int}} = 16\mathcal{M}$, $26\mathcal{M}$, $43\mathcal{M}$, and $62\mathcal{M}$, respectively. In the bottom panel, the integration surfaces are placed at $r_{\text{int}} = 20\mathcal{M}$, $27\mathcal{M}$, $44\mathcal{M}$, and $53\mathcal{M}$ for 2+1 simulation MP2a. For the outermost surfaces, we see deviations of less than a percent over the course of the entire evolution in each case, just as we did for the stationary puncture runs shown in Fig. 5.

behavior in the measured ADM mass. With regard to numerical resolution, we Richardson extrapolate using runs MP3a and MP3b measured at $r = 62\mathcal{M}$. Combined, we find an extrapolated value for the ADM mass of $M_{\text{ADM}} = 1.15615$, which falls within 10^{-4} of the analytic value computed using Eq. (14) for these approximate initial data.

For our 3+1 simulations we also compute the linear momentum from Eq. (15). In the top panel of Fig. 10, we show the linear momentum as a function of time, calculated at surfaces placed at radii $r_{\text{int}} = 26.8\mathcal{M}$. In general, we see excellent agreement with the exact analytic value up until $t \sim r_{\text{int}}$, for the reasons noted above. Recall that we adopt initial data for moving BHs that are analytic but approximate, since they solve the constraint equations only to order P^2 . The resulting error represents “junk” that propagates from the strong-field region outwards, and reaching the integration surface r_{int} at approximately $t \sim r_{\text{int}}$. Eq. (15) for the linear momentum also assumes that the coordinate vector pointing in the direction of the momentum is a Killing vector of the asymptotic, conformally related metric (see Appendix A of [78]); this assumption breaks down once the “junk” reaches r_{int} . Accordingly, evaluating Eq. (15) leads to an error in the linear momentum, as is evident from Fig. 10.

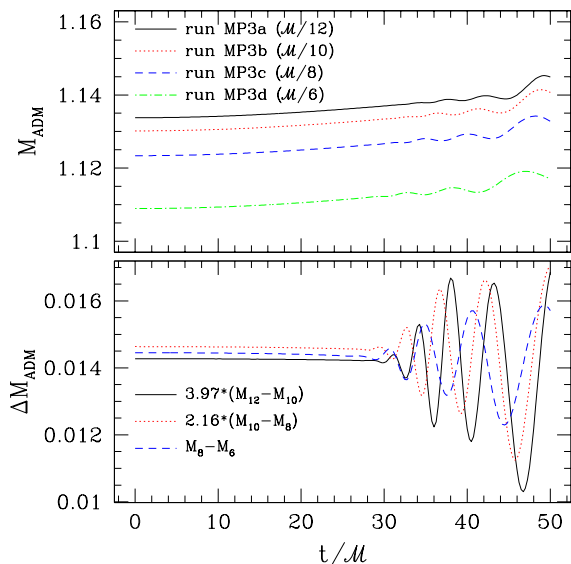


FIG. 9: ADM mass versus time for moving puncture evolutions MP3 (see Table II), for runs with different numerical resolutions (top panel). In each case, the integration surface was placed at $r = 62\mathcal{M}$. In the bottom panel, we show the differences in the measured ADM mass between pairs of “neighboring” resolution, scaled to reflect the second-order convergence.

In the bottom panel of the figure, we show the convergence behavior of the linear momentum. As for the ADM mass we find larger error terms once numerical errors reach the integration surface r_{int} .

As a further test we compare our numerical results for the lapse function α in runs MP2a and MP2c with those obtained by the numerical relativity group at NASA’s Goddard Space Flight Center ([71], hereafter GSFC). In Fig. 11 we graph α along the trajectory of the puncture at $t = 40\mathcal{M}$. The simulations of GSFC was performed using a numerical resolution of $\mathcal{M}/16$, but features a fourth-order accurate differencing scheme. We nevertheless find excellent agreement between our results.

Extending our tests to the 3+1 moving puncture cases, we show in the top panel of Fig. 12 the lapse function along the axis on which the BH travels, at $t = 20\mathcal{M}$. In the bottom panel, we show the convergence of the lapse function by taking the difference between the runs and rescaling to second-order, finding good agreement throughout. The slight discrepancy near the puncture position is due to the fact that there is a sharp trough in the lapse function there, but the position of the puncture itself falls at slightly different coordinate positions for the three runs. Indeed, since the shift vector, like all field quantities, is second-order convergent in the numerical resolution, so too is the speed at which the puncture moves, since $dx^i/dt = -\beta^i(x^i)$.

Turning our attention to the position of the puncture, we show in Fig. 13 the position of the BH puncture versus time in our three axisymmetric calculations performed at

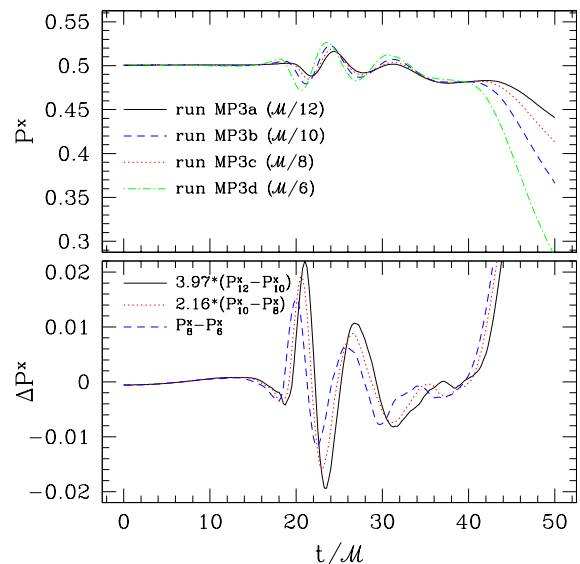


FIG. 10: The top panel shows the linear momentum P_x (Eq. (15)) evaluated at $r_{\text{int}} = 26\mathcal{M}$ for our simulations MP3. In the bottom panel, we show the difference between the values computed with different numerical resolutions, scaling the differences between the more accurate runs by factors of 3.97 and 2.16, as in Fig. 9, to highlight the second-order convergence of our code.

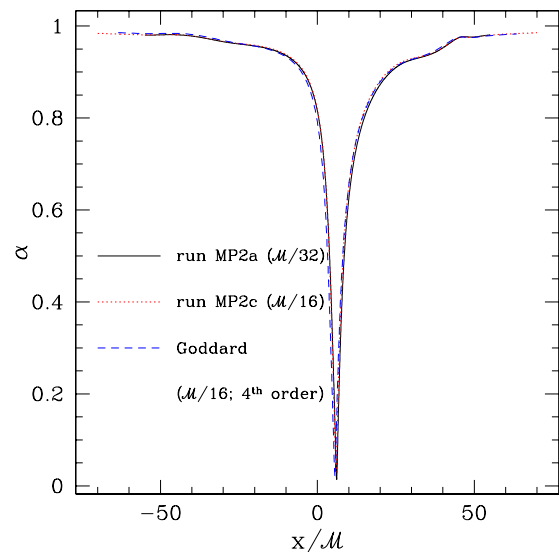


FIG. 11: Lapse function α shown at $T = 40\mathcal{M}$ along the path traveled by the moving puncture, for our axisymmetric 2+1 runs with numerical resolutions of $\mathcal{M}/32$ (run MP2a; dashed) and $\mathcal{M}/16$ (run MP2c; dotted), along with the numerical results of GSFC (solid) as discussed in [71]. The code used for the latter has numerical resolution $\mathcal{M}/16$, but uses fourth-order differencing, whereas we use a second order scheme.

different numerical resolutions, along with the Richardson extrapolation value. We see good agreement, and

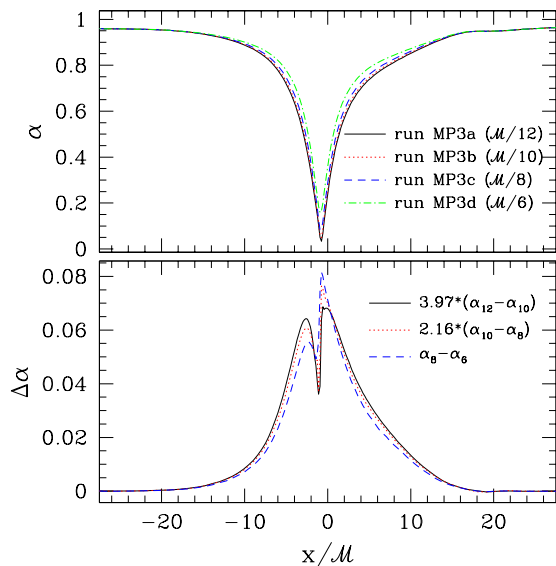


FIG. 12: The top panel shows the lapse function α measured on the x -axis, along which the puncture travels, at $t = 20\mathcal{M}$. In the bottom panel, we show the difference between the values computed with different numerical resolutions, rescaling the differences as in Fig. 9, to highlight the second-order convergence of our code.

note that numerical errors associated with coarser resolutions slow down the BH away from the proper asymptotic velocity. In the bottom panel of the figure, we show the difference in position versus time for our 2+1 runs, again suggesting second-order convergence.

IV. MATTER TESTS

In this Section we describe relativistic hydrodynamics simulations in the presence of puncture BHs. We are particularly interested in testing how the accretion of matter onto BHs can be simulated within the moving puncture approach. The exact Bondi solution for accretion onto a static Schwarzschild BH provides a perfect test bed for these purposes. A detailed discussion of the relativistic Bondi solution can be found in Appendix G of [79]; we summarize all relevant expressions in Appendix B. In Section IV A we test our code’s capability of simulating the accretion onto a static BH; in Section IV B we treat the identical problem, but viewed in a frame in which the BH is moving and represented by a moving puncture BH. We summarize our Bondi simulations in Table III.

A. Stationary Bondi solutions

The analytic solution describing Bondi accretion onto a stationary BH is usually given in Schwarzschild coordinates (see, e.g., Appendix G of [79] for a detailed description, and Appendix B 1 for a summary). To construct

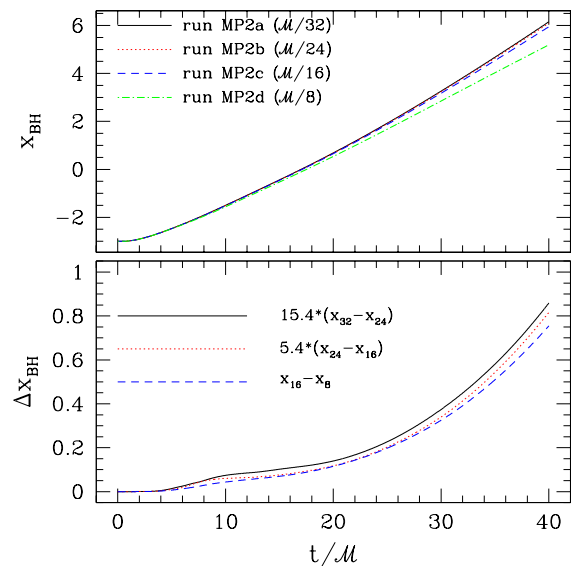


FIG. 13: Position of the BH puncture versus time for our 2+1 axisymmetric runs with numerical resolutions of $\mathcal{M}/32$ (run MP2a; solid), $\mathcal{M}/24$ (run MP2b; dotted), $\mathcal{M}/16$ (run MP2c; dashed), and $\mathcal{M}/8$ (run MP2d; dot-dashed). In the bottom panel, we show the difference in position versus time for the same runs, noting that we see second order convergence in the position of the puncture.

TABLE III: Summary of our matter evolution simulations. Key equations for the static Bondi solution, denoted by “SB”, are summarized in Appendix B. Moving Bondi solutions, constructed as described in Appendix B 3, are “boosted” to have a linear velocity $v^x = 0.1$

Name	Initial Data	Grid	Resolution	t_F
2+1 w/Fisheye; $ \bar{x}_{fish}^i \leq 15\mathcal{M}$, $ x^i \leq 136\mathcal{M}$				
SB2a	Static Bondi	360×360	$\mathcal{M}/24$	$100\mathcal{M}$
SB2b	Static Bondi	240×240	$\mathcal{M}/16$	$100\mathcal{M}$
SB2c	Static Bondi	120×120	$\mathcal{M}/8$	$100\mathcal{M}$
3+1 w/Fisheye; $ \bar{x}_{fish}^i \leq 10\mathcal{M}$, $ x^i \leq 56\mathcal{M}$				
SB3a	Static Bondi	$240^2 \times 120$	$\mathcal{M}/12$	$100\mathcal{M}$
SB3b	Static Bondi	$200^2 \times 100$	$\mathcal{M}/10$	$100\mathcal{M}$
SB3c	Static Bondi	$160^2 \times 80$	$\mathcal{M}/8$	$100\mathcal{M}$
SB3d	Static Bondi	$120^2 \times 60$	$\mathcal{M}/6$	$100\mathcal{M}$
3+1 w/Fisheye; $P^i = 0.1$, $ \bar{x}_{fish}^i \leq 10\mathcal{M}$, $ x^i \leq 56\mathcal{M}$				
MB3a	Moving Bondi	$240^2 \times 120$	$\mathcal{M}/12$	$100\mathcal{M}$
MB3b	Moving Bondi	$200^2 \times 100$	$\mathcal{M}/10$	$100\mathcal{M}$
MB3c	Moving Bondi	$160^2 \times 80$	$\mathcal{M}/8$	$100\mathcal{M}$
MB3d	Moving Bondi	$120^2 \times 60$	$\mathcal{M}/6$	$100\mathcal{M}$

initial data for our dynamical simulations, we transform this solution into isotropic coordinates, as described in Appendix B 2. Since isotropic coordinates become singular on the horizon at $r = \mathcal{M}/2$, so does the fluid velocity when expressed in these coordinates. We therefore adjust the fluid initial data artificially in the immediate vicinity

of the BH. Specifically, for the rest-mass density, we fit a quadratic function between $r = \mathcal{M}/2$ and $r = \mathcal{M}$ so that its radial derivative matches the analytic Bondi solution at $r = \mathcal{M}$ and the derivative goes to zero at $r = \mathcal{M}/2$. We note that for stationary BHs, $\mathcal{M} = M_{\text{ADM}}$. Inside the horizon at $r = \mathcal{M}/2$, we set the density equal to a small positive value at the origin, plus a term with radial dependence $\propto 1 - \cos(2\pi r/\mathcal{M})$ used to establish a smooth fit. For the velocity, we simply set $u = u|_{r=\mathcal{M}} \times (r/\mathcal{M})$ for $r < \mathcal{M}$. Since the flow is supersonic and directed inward, this does not affect the exterior solution, and even within $r < \mathcal{M}$ the fluid solution quickly settles into an equilibrium flow as our spacetime slicing evolves towards the late-time solution that penetrates the horizon smoothly.

To match to the stationary Bondi solution, in which the self-gravity of the gas is negligible, we require that the mass accretion rate multiplied by the integration time – which we choose to be $t_F = 100\mathcal{M}$ – remain small with respect to the mass of the BH. Thus, we set $\dot{M} = 10^{-4}$ for all runs shown here. We set the sonic areal radius to $r_s = 10\mathcal{M}$. The proper infall time required for the fluid to travel from $r \approx 9\mathcal{M}$ (r_s in isotropic radii) to the horizon at $r_h = \mathcal{M}/2$ is $23\mathcal{M}$, so that we evolve for just over four freefall times. The gas is at rest at infinity, with a uniform density of $\rho_\infty = 6.2 \times 10^{-8}$. The polytropic index is chosen to be $n = 3$ (thus, the adiabatic index is $\Gamma = 4/3$).

For the gauge conditions used in moving puncture simulations, the Bondi solution is not time-independent. Similarly to the vacuum solutions described in Section III, the evolution passes through a transient, time-dependent phase, and then settles down into a new equilibrium. This new equilibrium solution describes the usual Bondi solution, but expressed in a different coordinate system. To analyze this solution and compare it with the analytical solution (which is given in Schwarzschild coordinates), we therefore need to compare invariants.

One such invariant is the rate of change of the fluid rest density ρ_0 as measured by an observer moving with the fluid,

$$\dot{\rho}_0 \equiv d\rho_0/d\tau \equiv u^\mu \partial_\mu \rho_0, \quad (19)$$

where u^μ is the fluid's 4-velocity.

In Fig. 14, we show $d\rho_0/d\tau$ measured along the z -axis (perpendicular to the symmetry axis) as a function of the rest-mass density itself. In the top panel, we show the results for our highest resolution 3+1 simulation, run SB3a with $\mathcal{M}/12$ spacing, whereas in the bottom panel we plot values for run SB2a ($\mathcal{M}/24$). In both cases we plot the exact solution as points, along with our numerical profiles at $t = 20\mathcal{M}$, $t = 60\mathcal{M}$, and $t = 100\mathcal{M}$. We find good agreement throughout the evolution with variations of no more than 10% and 4% respectively for the 3+1 and 2+1 simulations.

As an additional test we compute the average areal

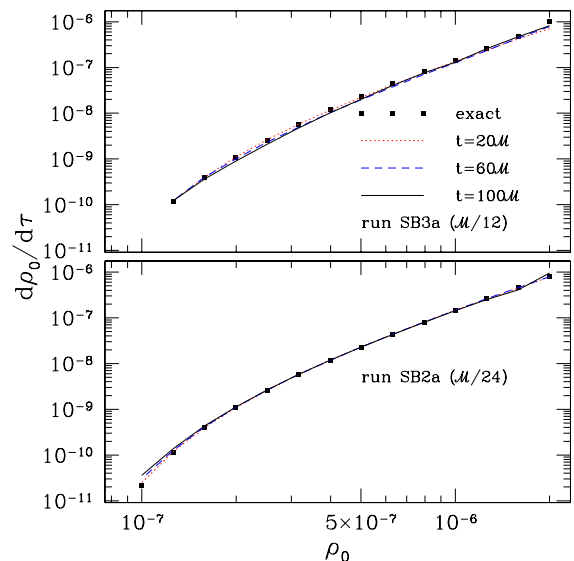


FIG. 14: Time rate of change of the rest-mass density, $d\rho_0/d\tau$, as a function of the rest-mass density. We show results for our highest resolution 3+1 (top panel) and 2+1 (bottom panel) calculations. The exact solution is represented by points, along with our profiles at $t = 20\mathcal{M}$ (dotted curve), $t = 60\mathcal{M}$ (dashed), and $t = 100\mathcal{M}$ (solid).

radius of isodensity surfaces, defined by

$$r_A \equiv \left(\frac{\mathcal{A}}{4\pi} \right)^{1/2}, \quad (20)$$

in terms of the surface's proper area \mathcal{A} . Evidently, this is again a coordinate-independent quantity. For the essentially spherically symmetric isodensity surfaces considered in this Section the average radius must of course be equal to its local value, but the definition Eq. (20) generalizes to the non-spherical configurations in Section IV B. In Fig. 15, we show the average radii of the same isodensity surfaces described in Fig. 14, following the same conventions. We note that it is possible to spot the phase transition between subsonic and supersonic behavior at the sonic radius r_S , marked by an arrow, which causes a shift in the power-law index of the radius-density relation. We also marked the horizon at r_h with a second arrow. Again, we see that the results are stable for a long period, with variations of no more than 5% and 3%, respectively.

To test the convergence of our implementation of relativistic hydrodynamics we have performed Bondi evolution calculations using the same set of numerical resolutions used previously for the vacuum puncture calculations described in Sec. III B. In Fig. 16, we show r_A for runs with differing numerical resolutions at the same fixed density value, chosen to be $\rho_0 = 3.8 \times 10^{-7}$, which lies near the center of our logarithmic range and corresponds to a location close to the sonic radius. We see that matter variables converge to second order in the grid

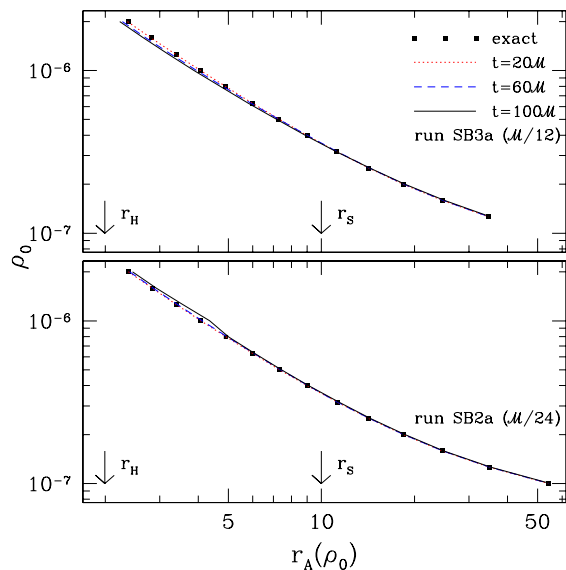


FIG. 15: Rest-mass density as a function of the areal radius of the corresponding isodensity surface, shown on a log-log scale. We show both our highest resolution 3+1 run (run SB3a; top panel) and 2+1 run (run SB2a; bottom panel). The density values at which we compute the surfaces are the same as in Fig. 14, as are all other conventions, though we note that the density axis have been flipped. We mark the BH horizon r_h and the sonic point of the flow r_s with arrows, noting that we can see evidence for the well-known phase transition in the density-radius relation at the sonic point.

resolution, just as the field variables do. In Fig. 16, we note that the extrapolated solution does seem to expand slowly over time, but that this effect represents approximately a 1% change over a period of $t = 100M$. This effect is caused by the presence of the outer boundary. At sufficiently early times, our numerical solution converges to the analytical solution in regions that are causally disconnected from the outer boundary.

As we discussed in Section II C, the point $r = 0$ corresponds to a surface of finite, positive areal radius (see [40, 41]), and represents a coordinate singularity only. Matter reaching this point therefore represents matter crossing a surface of a certain finite areal radius inside the horizon. Accordingly, all fluid quantities should remain finite at $r = 0$. In the top panel of Fig. 17, we show the rest-mass density as a function of areal radius for our highest-resolution 3+1 stationary Bondi result at different times, along with the analytical solution. We eliminate from the figure the three innermost grid points, where the hydrodynamical “fix” we apply (recall Sec. II E) directly affects the values of the primitive hydrodynamical variables computed from the conserved set. We see that the flow extends smoothly within the horizon, extending inward to nearly the asymptotic limiting value of $r_A = 1.31M$ [40]. Thus, the matter maintains a regular flow pattern into the BH, as we would expect, remaining finite and well-behaved indefinitely. In the bot-

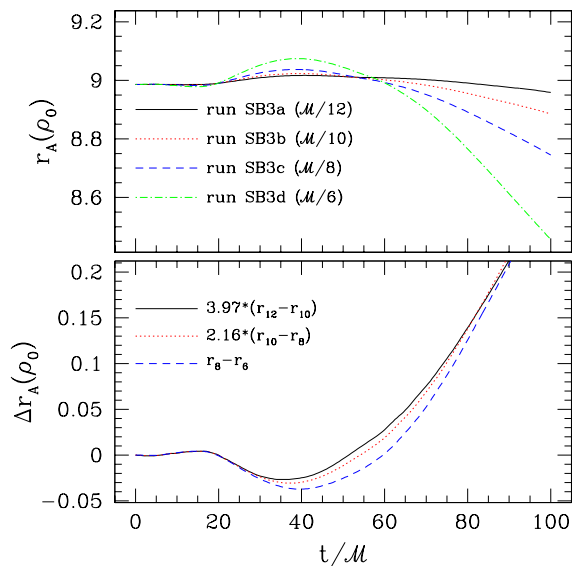


FIG. 16: The average areal radius of an isodensity surface with density $\rho_0 = 3.8 \times 10^{-7}$ as a function of time for 3+1 runs with different numerical resolutions: runs SB3a ($M/12$; solid), SB3b ($M/10$; dotted), SB3c ($M/8$; dashed), and SB3d ($M/6$; dot-dashed). In the bottom panel, we show the pairwise differences between runs.

tom panel of the figure, we show results at $t = 100M$ for runs of varying resolution, showing that we converge toward the analytic solution as we increase our numerical resolution, and that the physical region affected by the hydrodynamical fixes decreases in size as the resolution increases. We find the convergence is second-order at larger radii, and approximately first-order nearer the puncture where differencing errors across the puncture and the hydrodynamical fixes impose small-scale oscillations in the density.

B. Bondi solutions for moving punctures

We would also like to study our code’s ability to handle matter in the presence of a moving puncture. For these purposes we study the Bondi solution as viewed in a frame in which the Schwarzschild BH puncture is moving. Our method is described in Appendix B 3.

In this Section we consider BHs with a velocity of $v^x \equiv P^x/M = 0.1$, and let the BH start at a coordinate location of $x = -2.5M$. As in the stationary Bondi case discussed in Sec. IV A above, we evolve our 3+1 calculations for a duration $t = 100M$, equivalent to approximately 4 sonic radius freefall times, at which point the BH has moved to a coordinate location of $x = 1.8M$. To visualize the resulting evolution, we show density contours with overlaid arrows representing the velocity field at $t = 50M$ and $100M$ for run MB3a in Fig. 18. We see a clear pattern of translation as the entire solution evolves.

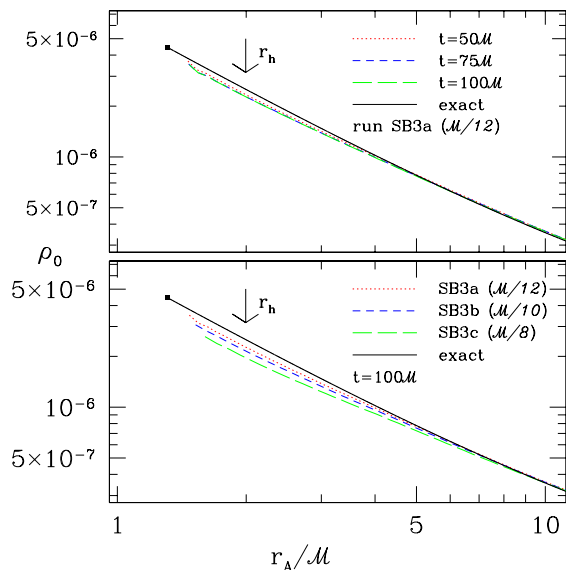


FIG. 17: The top panel shows the rest-mass density ρ_0 as a function of areal radius r_A for run SB3a at times $t = 50M$ (dotted), $t = 75M$ (dashed), and $t = 100M$ (dot-dashed), as well as the exact Bondi solution (solid). We exclude the three innermost gridpoints from each run, which are directly affected by our hydrodynamical “fixes”. We see the solution remains smooth and accurate across the horizon, at $r_A = r_h = 2M$, which is marked with an arrow, remaining finite everywhere and nearly constant in time. In the bottom panel of the figure we show results at $t = 100M$ for runs with three different numerical resolutions, showing the expected convergence toward the exact solution.

In Fig. 19 we show r_A as in Eq. (20), and $d\rho_0/d\tau$ from Eq. (19) as a function of density ρ_0 for simulation MB3a, our highest resolution moving Bondi run (compare Figs. 14 and 15 for stationary Bondi solutions). As before, the exact solutions are given by the points. We find that r_A agrees with the analytical solution to within about 3%. The co-moving time derivative of the density $d\rho_0/d\tau$, on the other hand, shows larger deviations of up to 20%. In Fig. 20, we show the convergence behavior in the average areal radius of the isodensity surfaces as a function of time for our runs, following the same conventions as Fig. 16. We see the same convergent behavior as in the vacuum and stationary Bondi cases: second-order convergence followed by the appearance of higher-order correction terms at approximately $t = 40M$.

V. DISCUSSION AND FUTURE CALCULATIONS

In this paper we have performed several test simulations involving the modeling of BHs within the moving puncture approach, both in vacuum and in the presence of a relativistic fluid.

Our vacuum tests focus on evolutions of both station-

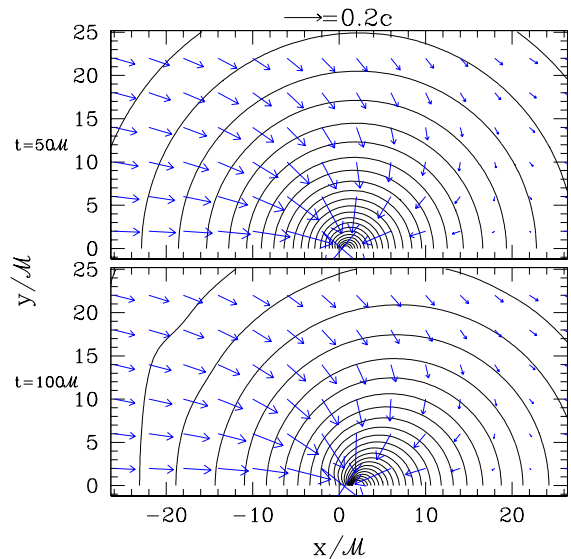


FIG. 18: Contours of the rest-mass density for our moving Bondi evolution run MB3a, shown as slices through the equatorial plane at $t = 50$ (top panel) and $t = 100M$ (bottom panel). Our simulation extends to cover the negative y -plane as well, but is visually indistinguishable from being completely symmetric. Density contours begin at $\rho_0 = 10^{-7}$, and are spaced logarithmically, 16 per decade. A velocity vector representing a magnitude $v = 0.2c$ is shown above the figure for reference.

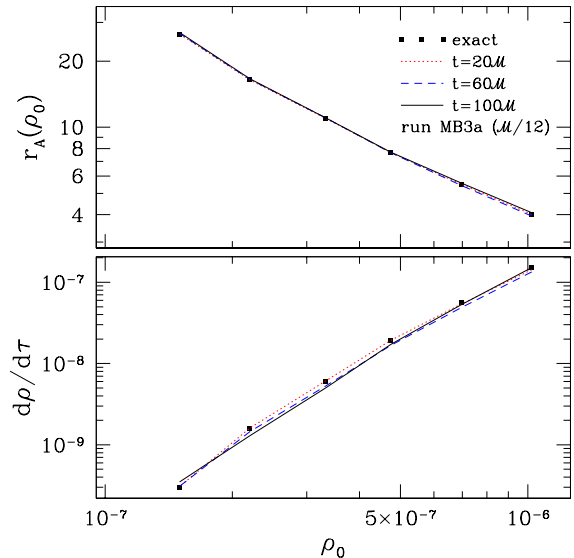


FIG. 19: Average proper radius of isodensity surfaces r_A (top panel) and time rate of change of the density along the z -axis, $d\rho_0/d\tau$, (bottom panel) shown as a function of the rest mass density on a log-log scale for run MB3a. The exact solutions are shown as square points. Results are shown at $t = 20M$ (dotted), $t = 60M$ (dashed), and $t = 100M$ (solid).

ary and moving BHs. We find that the code is second-

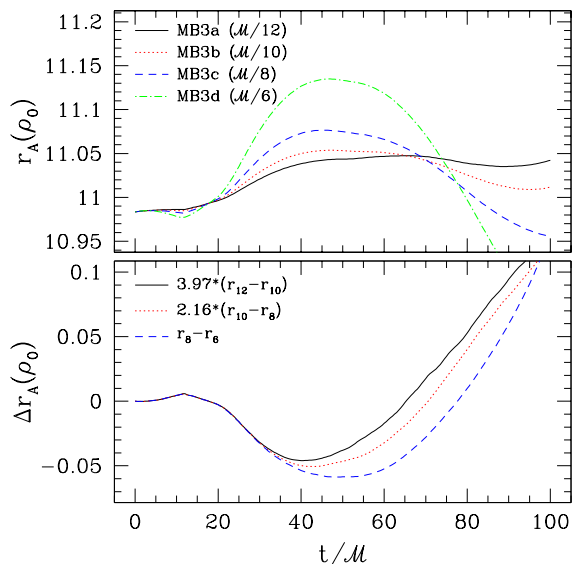


FIG. 20: The average areal radius r_A of the isodensity surface with density $\rho_0 = 3.8 \times 10^{-7}$ as a function of time (top panel) for runs with different numerical resolutions: runs MB3a ($\mathcal{M}/12$; solid), MB3b ($\mathcal{M}/10$; dotted), MB3c ($\mathcal{M}/8$; dashed), and MB3d ($\mathcal{M}/6$; dot-dashed). In the bottom panel, we show the scaled pairwise differences between the runs.

order convergent, as expected, but is limited primarily by the maximum numerical resolution we can achieve with our current second-order formulation (cf. the ADM mass convergence demonstrated in [30] at finer numerical resolution). To remedy this issue, we have introduced fourth-order spatial differencing into our code, results of which will be reported in [60]. We demonstrate that we can reproduce numerically the analytical solution of [44] for an isolated stationary BH, in line with previous studies of stationary isolated punctures (see, e.g., [23, 42, 43]). We also demonstrate that we can artificially modify the initial data in the BH interior, and even violate the constraints there, and still settle down to the same late-time asymptotic solution without significantly affecting the evolution in the BH exterior. While this result is not surprising, it is reassuring, and also has some implications for future simulations, as we discuss below.

To test the ability of the moving puncture approach to handle the flow of matter onto BHs, we study relativistic Bondi flow both for stationary and moving BHs and again compare with the analytic solution. Our findings demonstrate that all fluid variables remain regular throughout and do not need excision. This result can be understood in terms of the studies of [40, 41], who demonstrate that the puncture represents a limiting surface of finite areal radius, and hence a coordinate singularity only. Moving puncture evolutions never encounter the BH’s central spacetime singularity, and cover regular regions of the spacetime only. Hence all fluid invariants are regular throughout the puncture BH interior.

This paper represents a stepping-stone in our group’s

efforts to model relativistic BHNS binaries. We have previously constructed BHNS initial data, using the conformal thin-sandwich formalism and imposing quasi-equilibrium boundary conditions on the BH’s horizon (see [55, 56]). We have also performed preliminary dynamical simulations in conformal gravitation (see [47, 48]). We now plan to adopt the puncture method to simulate BHNS binaries fully self-consistently, similar to the calculations of [45, 46].

In contrast to [45, 46], we plan to evolve quasi-equilibrium conformal thin-sandwich initial data. This poses the conceptual problem that the initial data use excision to model the BH, while the dynamical evolution requires initial data everywhere. As shown above, however, our experiments with single BHs demonstrate that we can replace the initial data in the BH interior with arbitrary sufficiently smooth functions without significantly affecting the late-time solution, or the evolution, in the BH exterior. In fact, this suggests that moving puncture simulations of BHBH binaries may also use initial data constructed in the conformal thin-sandwich formalism (see, e.g., [57, 58]), which are believed to represent true quasi-equilibrium configurations more accurately [59]. The evolution of conformal thin-sandwich binary BH initial data will be considered in detail in a forthcoming paper [60].

Acknowledgments

It is a pleasure to thank Greg Cook, James van Meter, Carlos Lousto, Yuk Tung Liu, and Hwei-Jang Yo for helpful conversations. JAF is supported by an NSF Astronomy and Astrophysics Postdoctoral Fellowship under award AST-0401533. This work was supported in part by NSF grants PHY-0205155 and PHY-0345151 and NASA Grants NNG04GK54G and NNX07AG96G to the University of Illinois, and NSF Grant PHY-0456917 to Bowdoin College.

APPENDIX A: FISHEYE COORDINATES

Fisheye coordinates are defined through a purely radial coordinate transformation, in which we define a fisheye radius \bar{r} in terms of the physical radius r according to

$$\bar{r} = a_n r + \sum_{i=1}^n \frac{(a_{i-1} - a_i) s_i}{2 \tanh(R_i/s_i)} \ln \left(\frac{\cosh((r + R_i)/s_i)}{\cosh((r - R_i)/s_i)} \right), \quad (\text{A1})$$

(see Eqs. (3) and (4) of [19]). Here the a_i coefficients determine the “stretching” of the radial coordinate in several different regions, labeled by the i ’s, the R_i ’s define the center of transition zones between these regions, and the s_i ’s determine the width of these transition zones.

The derivative of this expression is given by

$$\frac{d\bar{r}}{dr} = a_n + \sum_{i=1}^n \frac{a_{i-1} - a_i}{\tanh(R_i/s_i)} \times \left(\frac{\tanh((r + R_i)/s_i) - \tanh((r - R_i)/s_i)}{2} \right), \quad (\text{A2})$$

which helps to understand how this transformation works. Assume that we arrange the R_i terms in such a way that neighboring transition zones do not overlap, i.e. $R_i - s_i > R_{i-1} + s_{i-1}$. Outside of the transition zones, i.e. for radii $R_{m-1} + s_{m-1} < r < R_m - s_m$, the derivative $d\bar{r}/dr$ is then given approximately by that region's coefficient a_{m-1} . This is because the last term in parentheses takes a value approximately equal to zero for all $i \leq m-1$ and approximately one for $i \geq m$. The fisheye transitions act in many ways like an effective fixed-mesh refinement, with spherical transitions separating regions with different resolutions. Angles with respect to the origin remain unchanged by the transformation, and spheres centered on the origin transform into spheres, albeit with a different radius. We always apply the fisheye transformation in terms of the origin of our coordinates, regardless of the position of the BH in cases where it is moving across the grid.

The fisheye transformation is purely radial. For Cartesian coordinates we define

$$\bar{x}^i = x^i \left(\frac{\bar{r}}{r} \right). \quad (\text{A3})$$

The Jacobian of the coordinate transformation and its inverse are given by

$$\frac{\partial x^i}{\partial \bar{x}^j} = \delta^i_j \left(\frac{r}{\bar{r}} \right) + \frac{\bar{x}^i \bar{x}^j}{\bar{r}^2} \left(\frac{dr}{d\bar{r}} - \frac{r}{\bar{r}} \right), \quad (\text{A4})$$

$$\frac{\partial \bar{x}^i}{\partial x^j} = \delta^i_j \left(\frac{\bar{r}}{r} \right) + \frac{\bar{x}^i \bar{x}^j}{\bar{r}^2} \left(\frac{d\bar{r}}{dr} - \frac{\bar{r}}{r} \right). \quad (\text{A5})$$

To construct initial data on a fisheye grid, the most direct method is to evaluate all quantities at the physical coordinates represented by the point, followed by an appropriate coordinate conversion. Since the transformation is purely spatial, all time-components of 4-vectors remain unaffected, and we can restrict the transformation to spatial components only, e.g.

$$\bar{v}^i = \frac{\partial \bar{x}^i}{\partial x^j} v^j; \quad \bar{v}_i = \frac{\partial x^j}{\partial \bar{x}^i} v_j, \quad (\text{A6})$$

and

$$\bar{\gamma}_{ij} = \frac{\partial x^l}{\partial \bar{x}^i} \frac{\partial x^m}{\partial \bar{x}^j} \gamma_{lm}. \quad (\text{A7})$$

The rest-density, for example, is the time-component of the fluid's density 4-vector, and is hence invariant under these transformations.

The determinant of the Jacobian is given by

$$J = \det(\partial x^i / \partial \bar{x}^j) = \left(\frac{r}{\bar{r}} \right)^2 \frac{dr}{d\bar{r}}. \quad (\text{A8})$$

We then have

$$\bar{\gamma} \equiv \det(\bar{\gamma}_j) = J^2 \gamma, \quad (\text{A9})$$

indicating that the determinant of the metric is a tensor density of weight 2. Using a conformal transformation $\gamma_{ij} = \psi^4 \tilde{\gamma}_{ij}$ so that the determinant of the conformally related metric is unity, $\tilde{\gamma} = 1$, implies

$$\bar{\psi}^{12} = J^2 \psi^{12}, \quad (\text{A10})$$

meaning that the conformal factor is a tensor density of weight 1/6. The conformal factor and its logarithm $\phi = \ln \psi$ then transform according to

$$\bar{\psi} = \left(\frac{r}{\bar{r}} \right)^{1/3} \left(\frac{dr}{d\bar{r}} \right)^{1/6} \psi, \quad (\text{A11})$$

$$\bar{\phi} \equiv \ln \bar{\psi} = \frac{1}{3} \ln \left(\frac{r}{\bar{r}} \right) + \frac{1}{6} \ln \left(\frac{dr}{d\bar{r}} \right) + \ln \psi. \quad (\text{A12})$$

Our conformal field quantities, $\tilde{\gamma}_{ij}$ and \tilde{A}_{ij} , both transform according to the relation,

$$\bar{\tilde{\gamma}}_{ij} = \left(\frac{r}{\bar{r}} \right)^{4/3} \left(\frac{dr}{d\bar{r}} \right)^{2/3} \frac{\partial x^l}{\partial \bar{x}^i} \frac{\partial x^m}{\partial \bar{x}^j} \tilde{\gamma}_{lm}. \quad (\text{A13})$$

The most complicated transformation is that of $\tilde{\Gamma}^i$, given by

$$\bar{\tilde{\Gamma}}^i = J^{2/3} \frac{\partial \bar{x}^j}{\partial x^i} \tilde{\Gamma}^i - \tilde{\gamma}^{ln} \left[-\frac{1}{2} \frac{\partial J^{2/3}}{\partial x^n} \frac{\partial \bar{x}^j}{\partial x^i} + J^{2/3} \frac{\partial^2 \bar{x}^j}{\partial x^i \partial x^n} \right]. \quad (\text{A14})$$

A time derivative of this term appears in the shift evolution equation (11b). Instead of evaluating this term exactly, we found it convenient to replace this equation with

$$\partial_t B^i = \left(\frac{dr}{d\bar{r}} \right)^2 \partial_t \bar{\tilde{\Gamma}}^i - \eta B^i, \quad (\text{A15})$$

since calculating the time derivative of the quantity $\tilde{\Gamma}^i$ requires taking a complicated spatially-varying linear combination of time derivatives of the spatial metric. Within the different fisheye regions (i.e. outside the transition zones), our expression reproduces the ‘‘non-shifting-shift’’ condition, and it is equivalent to Eq. (11b) in the area surrounding the BH itself. Elsewhere this modification affects only the coordinates, and not any physical quantities.

Due to the asymptotic behavior of various quantities in fisheye coordinates, we must modify our boundary conditions in some cases in order to reproduce the desired behavior in physical coordinates. In all cases where outgoing wavelike boundary conditions are used, we evaluate all radii in physical coordinates, not fisheye coordinates. The conformal factor ϕ , which does not asymptotically approach unity in fisheye coordinates, is converted into the physical coordinate expression using Eq. (A12), at which point boundary conditions are applied and the expression is converted back into fisheye.

APPENDIX B: THE RELATIVISTIC BONDI SOLUTION

A thorough derivation of the exact analytic relativistic Bondi solution may be found in Appendix G of [79]. Here we briefly review some of the basic features and most relevant equations. We assume that a BH of mass M is placed within an infinite cloud of gas that has a rest-mass density ρ_∞ and fluid 3-velocity $v^i = 0$ at spatial infinity, $r \rightarrow \infty$. We take the gas to be adiabatic with adiabatic index Γ . We can then solve the equations of relativistic hydrodynamics to find the stationary spherical accretion flow onto the black hole.

1. Review of key equations

For convenience, we will derive the equations determining the flow in Schwarzschild coordinates, and then convert these to the isotropic coordinates used throughout this paper. We denote Schwarzschild radii \hat{r} , the 4-velocity \hat{u}^α , and the inwardly directed radial component of the 4-velocity $\hat{u} \equiv -\hat{u}^r$. In terms of these we can recast the relativistic continuity and Euler equations in conserved form

$$4\pi\rho_0\hat{u}\hat{r}^2 \equiv \dot{M} = \text{const.} \quad (\text{B1})$$

$$h^2 \left(1 - \frac{2M}{\hat{r}} + \hat{u}^2 \right) \equiv h_\infty^2 = \text{const.} \quad (\text{B2})$$

Here we define the specific enthalpy $h \equiv 1 + \epsilon + P/\rho_0$ where ϵ is the internal energy of the fluid. We will assume a gamma-law equation of state

$$P = (\Gamma - 1)\rho_0\epsilon, \quad (\text{B3})$$

for which the enthalpy is $h = 1 + \Gamma\epsilon$. Inserting the latter into (B3) yields

$$P = (\Gamma - 1)\rho_0 \frac{h - 1}{\Gamma}. \quad (\text{B4})$$

For adiabatic flow the gamma-law equation of state (B3) implies the polytropic relation $P = \kappa\rho_0^\Gamma$, where κ is a constant. Combining this with (B4) yields

$$P = \kappa\rho_0^\Gamma = (\Gamma - 1)\rho_0 \left(\frac{h - 1}{\Gamma} \right). \quad (\text{B5})$$

For the gamma-law equation of state (EOS) (B3) the speed of sound is given by

$$a \equiv \frac{1}{h^{1/2}} \left(\frac{dP}{d\rho_0} \right)^{1/2} = \left(\frac{\Gamma P}{\rho_0 h} \right)^{1/2}. \quad (\text{B6})$$

Combining the above expressions we then find the following relations between the enthalpy and the speed of sound

$$a^2 = (\Gamma - 1) \frac{h - 1}{h}, \quad (\text{B7})$$

$$h = 1 + \frac{a^2}{\Gamma - 1 - a^2}. \quad (\text{B8})$$

All smooth solutions to the conservation laws (B1) and (B2) satisfying the EOS (B5) must pass through a sonic point, since the flow is subsonic at large radii but must be supersonic at the horizon. It can be shown that at the sonic point the radial velocity \hat{u}_s must satisfy

$$\hat{u}_s^2 = \frac{M}{2\hat{r}_s}, \quad (\text{B9})$$

and that the speed of sound at the sonic point is

$$a_s^2 = \frac{\hat{u}_s^2}{1 - 3\hat{u}_s^2}. \quad (\text{B10})$$

The accretion rate for the transonic solution is given uniquely by

$$\dot{M} = 4\pi\rho_s\hat{u}_s\hat{r}_s^2 = 4\pi\lambda_s M^2 \rho_\infty a_\infty^{-3}, \quad (\text{B11})$$

where ρ_∞ and a_∞ are the asymptotic density and sound speed, respectively, and $\lambda_s = \lambda_s(\Gamma)$ is tabulated in Table 14.1 of [79] for values $1 \leq \Gamma \leq 5/3$.

In Fig. 21, we show the particular Bondi solution we use throughout this paper, corresponding to a $\Gamma = 4/3$ EOS with a transonic flow satisfying $\dot{M} = 10^{-4}$ and $\hat{r}_s = 10M$ (for convenience, we set $M = 1$). In terms of these parameters, the polytropic constant is given by $\kappa = 7.56$, and the asymptotic rest-mass density by $\rho_\infty = 6.2 \times 10^{-8}$. In the top panel, we show the rest-mass density ρ_0 as a function of both Schwarzschild radius \hat{r} (dashed curve) and isotropic radius r (solid curve). Note that the isotropic solution terminates at $r_h = 0.5M$, since the interior Schwarzschild solution is mapped through the throat of the BH onto the other sheet of the topology. In the second panel, we show the value of u^0 as a function of the two coordinate radii, showing the divergence at the horizon. In the third panel, we show the radial component of the respective 4-velocities, $u(r)$ and $\hat{u}(\hat{r})$. Finally, in the bottom figure, we show the radial component of the 3-velocities, $v \equiv |v^r| = |u^r|/u^0$, seeing that in both cases this quantity goes to zero at the horizon, since the lapse vanishes there. We note, for clarity, that the rest-mass density ρ_0 and u remain finite and smooth through the horizon in the Schwarzschild metric, becoming singular only at the physical singularity at the origin. On the other hand, because of the coordinate singularities present in the Schwarzschild metric, the time-component of the 4-velocity u^0 and the radial 3-velocity v^r both diverge at the horizon.

2. Transformation to isotropic coordinates

To convert the Bondi solution from Schwarzschild to isotropic coordinates, we only need to transform the radii and velocities. The rest-mass density – as a time-component of the density 4-vector – is invariant under purely spatial coordinate transformations. The radial

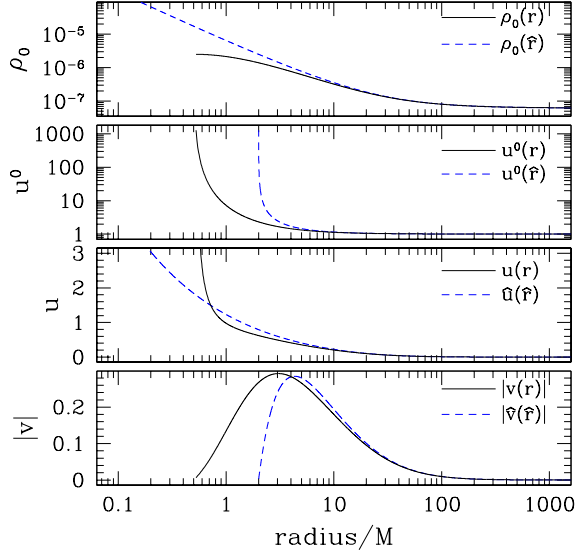


FIG. 21: The Bondi solution for matter accreting onto a BH, where we set the fluid EOS to be a $\Gamma = 4/3$ polytrope, the sonic radius as $\hat{r}_s = 10M$, and the mass accretion rate $\dot{M} = 10^{-4}$. In the top two panels, we show the rest-mass density and u^0 . Solid curves show the quantity as a function of isotropic radii, whereas dashed show Schwarzschild radii, with the transformation given by Eq. (B13). In the third panel, we show the radial component of the 4-velocity in both coordinate systems, with the transformation law given by Eq. (B14). In the bottom panel, we show the radial component of the 3-velocities for both coordinate systems. We note that $u^0 \rightarrow \infty$ and $v^i \rightarrow 0$ in either coordinate system as we approach the BH horizon, located at $r_h = 0.5M$ in isotropic coordinates and $\hat{r}_h = 2M$ is Schwarzschild.

transformation is given by

$$\hat{r} = r \left(1 + \frac{m}{2r}\right)^2, \quad (\text{B12})$$

$$r = \frac{\hat{r} - M + \sqrt{\hat{r}(\hat{r} - 2M)}}{2}. \quad (\text{B13})$$

Since the flow is purely radial, we have

$$\begin{aligned} u &= -u^r = -\hat{u}^{\hat{r}} \frac{dr}{d\hat{r}} = \hat{u} \left(\frac{d\hat{r}}{dr}\right)^{-1} \\ &= \frac{\hat{u}}{(1 - M/2r)(1 + M/2r)}. \end{aligned} \quad (\text{B14})$$

The 4-velocity's time-component u^0 remains unchanged under the transformation, which means that the radial component of the 3-velocity $v^r = u^r/u^0$ transforms in the same way as the that of the 4-velocity. We find the 3-velocity from the normalization

$$-\alpha^2(u^0)^2 + \psi^4(u^0)^2 v^2 = -1. \quad (\text{B15})$$

3. Moving Bondi solutions

One approach to construct a moving Bondi solution is to view the solution of the previous section from a frame in which the BH is moving and described by a moving BH puncture spacetime. Our strategy is to adopt a moving puncture spacetime and regular matter density and velocity profiles, with correct Bondi flow outer boundary conditions. We then allow the solution to come to steady-state and use invariant flow variables to compare with the stationary Bondi flow solution.

Specifically, we take the initial metric coefficients to be the vacuum moving puncture solution, as described in Sec. II B. We take the initial density at any coordinate point to be approximately the stationary isotropic Bondi solution. Finally, we compute the initial velocity field using the special-relativistic transformation law for velocities. Denoting the stationary Bondi solution with V , and assuming a “boost” velocity $v_b \equiv v_b^x$ in the x direction, we have

$$\frac{v^x}{c} = \frac{v_b^x + V^x}{1 + c^{-2}v_b^x V^x}, \quad (\text{B16})$$

$$\frac{v^y}{c} = \frac{V^y}{\gamma_b(1 + c^{-2}v_b^x V^x)}, \quad (\text{B17})$$

$$\frac{v^z}{c} = \frac{V^z}{\gamma_b(1 + c^{-2}v_b^x V^x)}, \quad (\text{B18})$$

where $\gamma_b \equiv (1 - v_b^2/c^2)^{-1/2}$ and the local value of the speed of light is $c \equiv \alpha/\psi^2$. Here, $v_b = P/M$, where P is the momentum of the puncture.

The resulting initial data matches the Bondi solution only approximately. However, all deviations propagate away quickly, leaving behind stationary Bondi flow onto a BH.

-
- [1] G. González and the LIGO Science Collaboration, ArXiv e-prints (2003), gr-qc/0303117.
 - [2] M. Ando and the TAMA collaboration, *Class. Quant. Grav.* **19**, 1409 (2002).
 - [3] M. Hewitson, P. Aufmuth, C. Aulbert, S. Babak, and R. Balasubramanian, *Class. Quant. Grav.* **20**, S581 (2003).
 - [4] A. Giazotto and S. Braccini, in *Recent developments*

in general relativity. 14th SIGRAV Conference on General Relativity and Gravitational Physics, Genova, Italy, September 18-22, 2000, edited by R. Cianci, R. Collina, M. Francaviglia, P. Fré. Milano: Springer (2002), pp. 111–119.

- [5] T. Prince, *AAS/High Energy Astrophysics Division* **8**, (2004).
- [6] E. Nakar, *Phys. Rep.* **442**, 166 (2007).

- [7] M. Shibata, K. Taniguchi, and K. Uryū, *Phys. Rev. D* **68**, 084020 (2003).
- [8] M. Shibata, K. Taniguchi, and K. Uryū, *Phys. Rev. D* **71**, 084021 (2005).
- [9] P. Marronetti, M. D. Duez, S. L. Shapiro, and T. W. Baumgarte, *Phys. Rev. Lett.* **92**, 141101 (2004).
- [10] M. Shibata and K. Taniguchi, *Phys. Rev. D* **73**, 064027 (2006).
- [11] M. D. Duez, Y. T. Liu, S. L. Shapiro, M. Shibata, and B. C. Stephens, *ArXiv e-prints* (2007), gr-qc/0701145.
- [12] B. C. Stephens, M. D. Duez, Y. T. Liu, S. L. Shapiro, and M. Shibata, *ArXiv e-prints* (2007), astro-ph/0702080.
- [13] M. Shibata, Y. T. Liu, S. L. Shapiro, and B. C. Stephens, *Phys. Rev. D* **74**, 104026 (2006).
- [14] F. Pretorius, *Phys. Rev. Lett.* **95**, 121101 (2005).
- [15] M. Campanelli, C. O. Lousto, P. Marronetti, and Y. Zlochower, *Phys. Rev. Lett.* **96**, 111101 (2006).
- [16] J. G. Baker, J. Centrella, D.-I. Choi, M. Koppitz, and J. van Meter, *Phys. Rev. Lett.* **96**, 111102 (2006).
- [17] M. Shibata and T. Nakamura, *Phys. Rev. D* **52**, 5428 (1995).
- [18] T. W. Baumgarte and S. L. Shapiro, *Phys. Rev. D* **59**, 024007 (1998).
- [19] M. Campanelli, C. O. Lousto, and Y. Zlochower, *Phys. Rev. D* **73**, 061501(R) (2006).
- [20] J. G. Baker, J. Centrella, D.-I. Choi, M. Koppitz, and J. van Meter, *Phys. Rev. D* **73**, 104002 (2006).
- [21] J. G. Baker, J. R. van Meter, S. T. McWilliams, J. Centrella, and B. J. Kelly, *ArXiv e-prints* (2006), gr-qc/0612024.
- [22] J. G. Baker, S. T. McWilliams, J. R. van Meter, J. Centrella, D.-I. Choi, B. J. Kelly, and M. Koppitz, *Phys. Rev. D* **75**, 124024 (2007).
- [23] B. Bruegmann, J. A. González, M. Hannam, S. Husa, U. Sperhake, and W. Tichy, *Phys. Rev. D* **76**, 061502 (2007).
- [24] J. G. Baker, J. Centrella, D.-I. Choi, M. Koppitz, J. R. van Meter, and M. C. Miller, *Astrophys. J. Lett.* **653**, L93 (2006).
- [25] F. Herrmann, I. Hinder, D. Shoemaker, and P. Laguna, *Class. Quant. Grav.* **24**, S33 (2007).
- [26] J. A. González, U. Sperhake, B. Brügmann, M. Hannam, and S. Husa, *Phys. Rev. Lett.* **98**, 091101 (2007).
- [27] M. Campanelli, C. O. Lousto, and Y. Zlochower, *Phys. Rev. D* **74**, 041501(R) (2006).
- [28] M. Campanelli, C. O. Lousto, and Y. Zlochower, *Phys. Rev. D* **74**, 084023 (2006).
- [29] F. Herrmann, I. Hinder, D. Shoemaker, P. Laguna, and R. A. Matzner, *Astrophys. J.* **661**, 430 (2007).
- [30] P. Marronetti, W. Tichy, B. Brügmann, J. González, M. Hannam, S. Husa, and U. Sperhake, *Class. Quant. Grav.* **24**, S43 (2007).
- [31] M. Campanelli, C. O. Lousto, Y. Zlochower, B. Krishnan, and D. Merritt, *Phys. Rev. D* **75**, 064030 (2007).
- [32] J. A. González, M. Hannam, U. Sperhake, B. Brügmann, and S. Husa, *Phys. Rev. Lett.* **98**, 231101 (2007).
- [33] W. Tichy and P. Marronetti, *Phys. Rev. D* **76**, 061502 (2007).
- [34] M. Campanelli, C. Lousto, Y. Zlochower, and D. Merritt, *Astrophys. J. Lett.* **659**, L5 (2007).
- [35] J. G. Baker, W. D. Boggs, J. Centrella, B. J. Kelly, S. T. McWilliams, M. C. Miller, and J. R. van Meter, *ArXiv e-prints* (2007), astro-ph/0702390.
- [36] F. Pretorius, *Class. Quant. Grav.* **23**, S529 (2005).
- [37] A. Buonanno, G. B. Cook, and F. Pretorius, *Phys. Rev. D* **75**, 124018 (2007).
- [38] M. A. Scheel, H. P. Pfeiffer, L. Lindblom, L. E. Kidder, O. Rinne, and S. A. Teukolsky, *Phys. Rev. D* **74**, 104006 (2006).
- [39] H. P. Pfeiffer, D. A. Brown, L. E. Kidder, L. Lindblom, G. Lovelace, and M. A. Scheel, *Class. Quant. Grav.* **24**, S59 (2007).
- [40] M. Hannam, S. Husa, D. Pollney, B. Brügmann, and N. Ó Murchadha, *ArXiv e-prints* (2006), gr-qc/0606099.
- [41] M. Hannam, S. Husa, B. Brügmann, J. A. González, U. Sperhake, and N. Ó Murchadha, *J. Phys. Conf. Series* **66**, 012047 (2007).
- [42] J. D. Brown, *ArXiv e-prints* **705** (2007), 0705.1359.
- [43] D. Brown, *ArXiv e-prints* **705** (2007), 0705.3845.
- [44] T. W. Baumgarte and S. G. Naculich, *Phys. Rev. D* **75**, 067502 (2007).
- [45] M. Shibata and K. Uryu, *Class. Quant. Grav.* **24**, S125 (2007).
- [46] M. Shibata and K. Uryū, *Phys. Rev. D* **74**, 121503(R) (2006).
- [47] J. A. Faber, T. W. Baumgarte, S. L. Shapiro, and K. Taniguchi, *Astrophys. J. Lett.* **641**, L93 (2006).
- [48] J. A. Faber, T. W. Baumgarte, S. L. Shapiro, K. Taniguchi, and F. A. Rasio, *Phys. Rev. D* **73**, 024012 (2006).
- [49] F. Löffler, L. Rezzolla, and M. Ansorg, *Phys. Rev. D* **74**, 104018 (2006).
- [50] E. Rantsiou, S. Kobayashi, P. Laguna, and F. Rasio, *ArXiv e-prints* (2007), astro-ph/0703599.
- [51] L. Baiotti and L. Rezzolla, *Phys. Rev. Lett.* **97**, 141101 (2006).
- [52] L. Baiotti, I. Hawke, and L. Rezzolla, *Class. Quant. Grav.* **24**, S187 (2007).
- [53] T. W. Baumgarte, M. L. Skoge, and S. L. Shapiro, *Phys. Rev. D* **70**, 064040 (2004).
- [54] K. Taniguchi, T. W. Baumgarte, J. A. Faber, and S. L. Shapiro, *Phys. Rev. D* **72**, 044008 (2005).
- [55] K. Taniguchi, T. W. Baumgarte, J. A. Faber, and S. L. Shapiro, *Phys. Rev. D* **74**, 041502(R) (2006).
- [56] K. Taniguchi, T. W. Baumgarte, J. A. Faber, and S. L. Shapiro, *Phys. Rev. D* **75**, 084005 (2007).
- [57] G. B. Cook and H. P. Pfeiffer, *Phys. Rev. D* **70**, 104016 (2004).
- [58] M. Caudill, G. B. Cook, J. D. Grigsby, and H. P. Pfeiffer, *Phys. Rev. D* **74**, 064011 (2006).
- [59] E. Berti, S. Iyer, and C. M. Will, *Phys. Rev. D* **74**, 061503(R) (2006).
- [60] Z. B. Etienne, J. A. Faber, Y. T. Liu, S. L. Shapiro, and T. W. Baumgarte, *Phys. Rev. D* (2007), accepted; arXiv:0707.2083.
- [61] M. D. Duez, P. Marronetti, S. L. Shapiro, and T. W. Baumgarte, *Phys. Rev. D* **67**, 024004 (2003).
- [62] R. Beig and N. Ó Murchadha, *Class. Quant. Grav.* **11**, 419 (1994).
- [63] R. Beig and N. Ó Murchadha, *Class. Quant. Grav.* **13**, 739 (1996).
- [64] S. Brandt and B. Brügmann, *Phys. Rev. Lett.* **78**, 3606 (1997).
- [65] G. B. Cook, *Living Rev. Rel.* **5**, 1 (2000).
- [66] T. W. Baumgarte and S. L. Shapiro, *Phys. Rept.* **376**, 41 (2003).
- [67] P. Laguna, *Phys. Rev. D* **69**, 104020 (2004).

- [68] B. Brügmann, *Int. J. Mod. Phys. D* **8**, 85 (1999).
- [69] M. Alcubierre, W. Benger, B. Brügmann, G. Lanfermann, L. Nерger, E. Seidel, and R. Takahashi, *Phys. Rev. Lett.* **87**, 271103 (2001).
- [70] M. Shibata, *Prog. Theor. Phys.* **101**, 1199 (1999).
- [71] J. R. van Meter, J. G. Baker, M. Koppitz, and D.-I. Choi, *Phys. Rev. D* **73**, 124011 (2006).
- [72] C. Gundlach and J. M. Martín-García, *Phys. Rev. D* **74**, 024016 (2006).
- [73] M. D. Duez, Y. T. Liu, S. L. Shapiro, and B. C. Stephens, *Phys. Rev. D* **72**, 024028 (2005).
- [74] <http://www.cactuscode.org/>.
- [75] M. Alcubierre, B. Brügmann, D. Holz, R. Takahashi, S. Brandt, E. Seidel, J. Thornburg, and A. Ashtekar, *International Journal of Modern Physics D* **10**, 273 (2001).
- [76] K. A. Dennison, T. W. Baumgarte, and H. P. Pfeiffer, *Phys. Rev. D* **74**, 064016 (2006).
- [77] M. Alcubierre, S. Brandt, B. Brügmann, C. Gundlach, J. Massó, E. Seidel, and P. Walker, *Class. Quant. Grav.* **17**, 2159 (2000).
- [78] G. B. Cook, *Phys. Rev. D* **50**, 5025 (1994).
- [79] S. L. Shapiro and S. A. Teukolsky, *Black Holes, White Dwarfs and Neutron Stars: The Physics of Compact Objects* (Wiley-VCH, 1986).